



University of  
Massachusetts  
Amherst

## Photofragment Imaging Fast Ion Beams

Item Type	Dissertation (Open Access)
Authors	Johnston, Michael D.
DOI	<a href="https://doi.org/10.7275/11599715.0">10.7275/11599715.0</a>
Download date	2026-05-17 21:08:20
Link to Item	<a href="https://hdl.handle.net/20.500.14394/17449">https://hdl.handle.net/20.500.14394/17449</a>

**PHOTOFRAGMENT IMAGING FAST ION BEAMS**

A Dissertation Presented

by

MICHAEL D. JOHNSTON, JR.

Submitted to the Graduate School of the  
University of Massachusetts Amherst in partial fulfillment  
of the requirements for the degree of

DOCTOR OF PHILOSOPHY

May 2018

Department of Chemistry

© Copyright by Michael D. Johnston, Jr. 2018

All Rights Reserved

# PHOTOFRAGMENT IMAGING FAST ION BEAMS

A Dissertation Presented

by

MICHAEL D. JOHNSTON, JR.

Approved as to style and content by:

---

Ricardo B. Metz, Chair

---

Bret E. Jackson, Member

---

Michael J. Maroney, Member

---

David M. Kawall, Member

---

Richard W. Vachet, Department Head  
Department of Chemistry

## **DEDICATION**

To my parents, for my means, and to Brittany, my inspiration.

## ACKNOWLEDGEMENTS

I would not have reached this stage of my personal and professional development without the support of many people; if I have seen far, it is because I stood on their shoulders. I have been influenced by many outstanding educators since my early school years who have passed their passion for science and love of learning onto me through their teaching. I owe tremendous gratitude to my advisor, mentor, and friend, Rick Metz, whose vision and leadership has been the guiding force behind the completion of this project. The breadth of knowledge that I have gained from working in the Metz lab is vast and extends far beyond the field of chemistry. It has undoubtedly made me a more well-rounded and better person. I would also like to thank my friend and former undergraduate advisor Gamil Guirgis, who was instrumental in my decision to pursue an advanced education.

I owe my thanks to Lee Pearson, who served as a mentor during my early days in the lab, and who contributed significantly to the design and early construction of the titular imaging instrument. I want to thank my coworkers and friends, Matt Gentry and Schuyler Lockwood, who contributed to the studies of manganese oxide and aluminum dimer, respectively. I would also like to extend my appreciation to Abdulkadir, Affawn, and Chris for many helpful comments, interesting conversations, and for making the lab a generally enjoyable place to work.

I thank the NSF for providing the funding for this research and the University of Massachusetts Amherst for the opportunity to pursue this degree.

Finally, I am especially grateful to my parents and to my wife, Brittany, for their endless love and support.

## ABSTRACT

### PHOTOFRAGMENT IMAGING FAST ION BEAMS

MAY 2018

MICHAEL D. JOHNSTON, JR., B.S., COLLEGE OF CHARLESTON

Ph.D., UNIVERSITY OF MASSACHUSETTS AMHERST

Directed by: Professor Ricardo B. Metz

Metal-containing ions have been the subject of much research due to their roles in catalytic activation and small cluster chemistries. However, they can be difficult to study both experimentally and theoretically, and new approaches are needed. The goal of the research described here is to characterize the electronic structures and thermodynamics of metal-containing ions using gas-phase spectroscopy experiments performed on a powerful new instrument. Presented in the following chapters are the details of a recently built velocity map imaging mass spectrometer that is capable of imaging the photofragments of trap-cooled ( $\geq 7\text{K}$ ) ions produced in a versatile ion source. This instrument has been used to study the predissociation of  $\text{N}_2\text{O}^+$  produced by electric discharge as well as the photodissociation of  $\text{Al}_2^+$  and  $\text{MnO}^+$  formed by laser ablation. The experimental resolution is currently limited by the diameter of the collimating iris to a value of  $\Delta v / v = 7.6\%$ . Photofragment images of  $\text{N}_2\text{O}^+$  show that when the predissociative state is changed from  $^2\Sigma^+(200)$  to  $^2\Sigma^+(300)$  the dominant product channel shifts from spin-forbidden ground state,  $\text{N}(^4\text{S}) + \text{NO}^+(v=5)$ , to a spin-allowed pathway,  $\text{N}^*(^2\text{D}) + \text{NO}^+$ . The first photofragment images of  $\text{Al}_2^+$  confirm the existence of a directly dissociative parallel transition ( $^2\Sigma_u^+ \leftarrow ^2\Sigma_g^+$ ) near  $23,250\text{ cm}^{-1}$  that yields products with a

large amount of kinetic energy. The  $D_0$  of ground state  $\text{Al}_2^+$  ( $^2\Sigma_g^+$ ) obtained from these images is  $138 \pm 5$  kJ/mol. At higher energy, above  $40,400\text{ cm}^{-1}$ , transitions are observed to a predissociative excited state, which calculations identify as the  $G\ ^2\Sigma_u^+$  state. The photodissociation spectrum of the  $G\ ^2\Sigma_u^+ \leftarrow X\ ^2\Sigma_g^+$  transition in  $\text{Al}_2^+$  gives an average vibrational spacing of  $170\text{ cm}^{-1}$  for the  $G\ ^2\Sigma_u^+$  state and  $\nu_0=172\text{ cm}^{-1}$  for the ground state ( $X\ ^2\Sigma_g^+$ ). Photofragment images from the  $G\ ^2\Sigma_u^+ \leftarrow X\ ^2\Sigma_g^+$  transition indicate that once the  $\text{Al}\ (^4\text{P}) + \text{Al}^+\ (^1\text{S})$  product channel is energetically accessible, it dominates the lower energy pathways despite being spin-forbidden. These images also yield a more precise  $D_0=136.6 \pm 1.8$  kJ/mol, highlighting the improved resolution achieved from imaging at near-threshold energies. For  $\text{MnO}^+$ , the photodissociation spectroscopy and images from  $21,300 - 33,900\text{ cm}^{-1}$  confirm the theoretical ground state ( $^5\Pi$ ) and give its bond dissociation energy ( $D_0=242 \pm 5$  kJ/mol). The spin-orbit constant of the dominant optically accessible excited state ( $^5\Pi^*$ ) in the region is also measured ( $A=22\text{ cm}^{-1}$ ). Photodissociation from this state is observed to proceed faster than the rotational period and result exclusively in ground state  $\text{Mn}^+\ (^7\text{S}) + \text{O}\ (^3\text{P})$  products. At energies above  $30,000\text{ cm}^{-1}$ , the  $\text{Mn}^{+*}\ (^5\text{S}) + \text{O}\ (^3\text{P})$  channel becomes the preferred dissociation pathway. Overall, imaging the photofragments of metal-containing ions can help elucidate their electronic structures and photodissociation dynamics, providing valuable experimental benchmarks for these often computationally challenging species.

## TABLE OF CONTENTS

	Page
ACKNOWLEDGEMENTS .....	v
ABSTRACT .....	vi
LIST OF TABLES .....	x
LIST OF FIGURES .....	xii
 CHAPTER	
1. INTRODUCTION .....	1
1.1 Motivations .....	1
1.2 Photodissociation Spectroscopy.....	2
1.3 Photofragment Imaging .....	4
1.4 References.....	5
2. EXPERIMENTAL.....	10
2.1 Introduction.....	10
2.2 Instrumental .....	12
2.2.1 Ion Source .....	12
2.2.2 Ion Trap.....	13
2.2.3 Beam Acceleration and Manipulation .....	16
2.2.4 Velocity Map Imaging .....	17
2.2.5 Data Acquisition and Processing .....	19
2.3 Preliminary Results: N <sub>2</sub> O <sup>+</sup> .....	21
2.4 Conclusions.....	23
2.5 References.....	24
3. THE ALUMINUM DIMER CATION .....	32
3.1 Introduction.....	32
3.2 Methods.....	34
3.3 Theoretical Electronic Structure of Al <sub>2</sub> <sup>+</sup> .....	35
3.4 Photodissociation Spectra of Al <sub>2</sub> <sup>+</sup> .....	36
3.5 Images of Al <sup>+</sup> Fragments .....	38
3.5.1 Images from (C <sup>2</sup> Σ <sub>u</sub> <sup>+</sup> ← X <sup>2</sup> Σ <sub>g</sub> <sup>+</sup> ).....	39
3.6.1 Images from (G <sup>2</sup> Σ <sub>u</sub> <sup>+</sup> ← X <sup>2</sup> Σ <sub>g</sub> <sup>+</sup> ).....	40

3.6	Conclusions.....	43
3.7	References.....	45
4.	THE MANGANESE OXIDE CATION.....	54
4.1	Introduction.....	54
4.2	Methods.....	55
4.3	Theoretical Electronic Structure of $\text{MnO}^+$ .....	56
4.4	Photodissociation Spectrum of $\text{MnO}^+$ .....	58
4.5	Images of $\text{Mn}^+$ Fragments.....	59
4.6	Conclusions.....	62
4.7	References.....	63
5.	CONCLUSIONS AND FUTURE DIRECTIONS.....	72
5.1	Conclusions.....	72
5.2	Future Directions.....	75
	BIBLIOGRAPHY.....	78

## LIST OF TABLES

Table	Page
3.1. Experimental and theoretical bond dissociation energies ( $D_0$ ) of $\text{Al}_2^+$ ( $^2\Sigma_g^+$ ).....	53
4.1. Experimental and theoretical bond dissociation energies ( $D_0$ ) of $\text{MnO}^+$ ( $^5\Pi$ ).....	71

## LIST OF FIGURES

Figure	Page
1.1. Potential energy surfaces depicting photon absorption by a cation ( $AB^+$ ) and the resulting photodissociation from an excited electronic state ( $AB^{+*}$ ) near the photoproduct ( $A + B^+$ ) threshold.....	7
1.2. Potential energy surfaces depicting photon absorption by a cation ( $AB^+$ ) and the resulting predissociation from an excited electronic state ( $AB^{+*}$ ) well above the photoproduct ( $A + B^+$ ) threshold .....	8
1.3. Potential energy surfaces depicting photon absorption by a cation ( $AB^+$ ) and the resulting photodissociation from a repulsive excited electronic state ( $AB^{+*}$ ) above the photoproduct ( $A + B^+$ ) threshold.....	9
2.1. Schematic overview of the fast ion photofragment imaging mass spectrometer .....	27
2.2. Detail of the ion source in laser ablation mode (top view) .....	28
2.3. Detail of the refrigerated ion trap assembly.....	29
2.4. Detail of the velocity map imaging ion optics (IO) showing the equipotential lines at 30 V intervals for optimized $Al_2^+$ settings (Generated using SIMION 7.0).....	30
2.5. Raw photofragment images of $NO^+$ made by dissociating $N_2O^+$ at 30,914 $cm^{-1}$ (top) and 32,238 $cm^{-1}$ (bottom) and their corresponding velocity distributions converted to total kinetic energy release.....	31
3.1. Relevant MRCI-F12/aug-cc-pVTZ calculated potential energy surfaces for excited states of $Al_2^+$ below 50,000 $cm^{-1}$ .....	47
3.2. Photodissociation spectrum of $Al_2^+$ in the $G^2\Sigma_u^+ \leftarrow X^2\Sigma_g^+$ transition region .....	48
3.3. Photofragment image of $Al^+$ made by dissociating $Al_2^+$ at 23,669 $cm^{-1}$ and the corresponding velocity distribution converted to total kinetic energy release.....	49
3.4. Photofragment image of $Al^+$ made by dissociating $Al_2^+$ at 39,703 $cm^{-1}$ and the corresponding velocity distribution converted to total kinetic energy release.....	50

3.5. Photofragment image of $\text{Al}^+$ made by dissociating $\text{Al}_2^+$ at $40,922 \text{ cm}^{-1}$ and the corresponding velocity distribution converted to total kinetic energy release.....	51
3.6. Plot of excitation energy versus total kinetic energy release for several images of $\text{Al}^+$ products resulting from photodissociation of cold $\text{Al}_2^+$ . .....	52
4.1. Potential energy curves for quintet states of $\text{MnO}^+$ calculated using TD-DFT with the B3LYP functional and 6-311++G(3df,3pd) basis set .....	64
4.2. Potential energy curves for quintet states of $\text{MnO}^+$ calculated using EOM-CCSD with the aug-cc-pVTZ basis set.....	65
4.3. Photodissociation spectrum of $\text{MnO}^+$ from $21,300 - 33,900 \text{ cm}^{-1}$ .....	66
4.4. Photodissociation spectrum of $\text{MnO}^+$ from $27,000 - 27,500 \text{ cm}^{-1}$ .....	67
4.5. Photofragment image of $\text{Mn}^+$ made by dissociating $\text{MnO}^+$ at $27,278 \text{ cm}^{-1}$ and the corresponding velocity distribution converted to total kinetic energy release.....	68
4.6. Photofragment image of $\text{Mn}^+$ made by dissociating $\text{MnO}^+$ at $30,488 \text{ cm}^{-1}$ and the corresponding velocity distribution converted to total kinetic energy release.....	69
4.7. Plot of excitation energy versus total kinetic energy release for several images of $\text{Mn}^+$ products resulting from photodissociation of cold $\text{MnO}^+$ .....	70

# CHAPTER 1

## INTRODUCTION

### 1.1 Motivations

The fundamental chemistry of transition metals and metal-containing compounds has been studied for decades and continues to remain at the forefront of scientific research as it relates to the catalytic activation of important raw materials and fuel sources. Many metal clusters, ions and their compounds with main group elements are known to activate C-H and C-C bonds in alkanes with varying efficiencies. Methane is a plentiful fuel and feedstock, so its conversion into other chemically useful compounds like methanol and long chain alkanes is of particular interest. Yet, efficient, large-scale methane activation remains an elusive goal.

Studies of transition metal catalyzed systems in the solid phase have increased our knowledge of catalytic chemistry over the years. However, the fundamental interactions that lie at the heart of these important chemical processes are still poorly defined in many cases. Unlike in the solid or liquid phases, the bonding in a free gaseous molecule or ion can be investigated without interference from its neighbors. Thus, gas-phase techniques like ion spectroscopy or reactions of guided ion beams can be an effective way of studying isolated interactions without the muddling effects of solvation or bulk phase phenomena.

More recently, modern quantum theory has been employed to model the chemistry of potential new catalysts and activation mechanisms. Accurate computational studies require highly specific mathematical models to generate meaningful results. The most rigorous computational methods are confirmed by large bases of experimental

benchmarks built around the chemical systems of choice. Metal-containing ions have proven difficult for theoretical approaches because of the many electrons and closely spaced electronic states that must be accounted for. Unfortunately, accurate and precise experimental values for these computationally challenging species are often limited due to the difficulty of studying them. In order to develop more detailed mathematical models that describe the complex chemistry of catalytic activation, it is necessary to continue to devise new experimental approaches and techniques that will increase our understanding of the most fundamental interactions between metal ions, clusters, and compounds.

## **1.2 Photodissociation Spectroscopy**

The fundamental properties that define chemistry are the behavior of electrons. Understanding how the electrons of a particular species behave when exposed to electromagnetic radiation or how they behave differently in the presence of another atom or atoms is key to understanding the chemistry of a particular system. Therefore, spectroscopy is generally an effective method for interrogating a chemical species of interest. Perhaps the most fundamental way to describe a chemical bond is by defining its strength. Physical properties like the bond dissociation energy ( $D_0$ ) offer quantified definitions of the interactions between electrons and atoms that can be compared to mathematically derived values as a measure of accuracy. So, in order to experimentally determine spectroscopic and electronic properties like bond strength, it is helpful to study how a molecule or ion falls apart when exposed to light; this is called photodissociation spectroscopy.

Photodissociation spectroscopy has been used to investigate the bonding and electronic structure of many interesting ligated transition metal ions.<sup>1-5</sup> It can be used to gain insight about important properties like excited state energies, vibrational frequencies and bond lengths. However, this powerful technique's ability to measure bond strengths can be limited by the inherent electronic structure of some would-be analytes. For example, in order to determine an accurate  $D_0$  in a typical photodissociation spectroscopy experiment, the energy of the photolysis laser is slowly increased until dissociation of the parent ion is observed. The photon energy at which the fragments are first observed is, at the very least, a rigorous upper limit to the bond dissociation energy. If the potential energy surface (PES) of the initially excited predissociative electronic state lies partially within the bound potential of the ground state (Figure 1.1), then the onset of dissociation is thermodynamic, and the measured bond strength is quite accurate.<sup>6</sup> However, many metal-containing ions do not have electronic structures that conform to this convenient model.

In some cases, the first optically accessible electronic excited state lies well above the first onset of dissociation (Figure 1.2). In this example, the photon energy when fragmentation is first observed only represents an upper limit to the bond strength and the onset measured is spectroscopic rather than thermodynamic. Precisely defining the  $D_0$  by photodissociation spectroscopy may not be possible for an analyte with such an electronic structure. However, other important properties like rotational and vibrational frequencies may still be obtained from the photodissociation spectrum, yielding valuable insight into the geometry and connectivity of the parent ion.

In the final case, the optically excited transition may be to an unbound state (Figure 1.3). In such a situation, the analyte will absorb over a broad spectral range, resulting in an unstructured photodissociation spectrum that provides little or no useful information. Ions that undergo optical transitions to repulsive states at lower energies may have more spectroscopically useful states at higher energies, near the onsets of dissociation for electronically excited fragments. Unfortunately, traditional photodissociation spectroscopy can have trouble differentiating between photoproducts based solely on internal energy and new onsets may be difficult to identify. It is therefore necessary to implement complementary techniques that will facilitate the precise measurement of dissociation energies for the more challenging cases described above.

### **1.3 Photofragment Imaging**

When a singly charged cation absorbs a photon with energy in excess of the bond dissociation energy, the cation can dissociate, yielding a charged fragment and a neutral cofragment. If this occurs, the energy that remains after bond breaking must be partitioned among the remaining degrees of freedom. The fragments can carry away internal energy in the form of excited rotational, vibrational, and electronic states. They will likely also depart with some amount of translational motion. If photodissociation occurs above the energetic threshold to form internally excited fragments, then some distribution of all the accessible states will be populated. So, for each combination of populated fragment states, a different amount of energy will remain and be manifested as kinetic energy.

Using this principle, photofragment imaging was developed<sup>7</sup> as a two-dimensional method to differentiate between the fragments of photolysis events based on their unique kinetic energy releases (KER). This gives one the ability to measure bond dissociation energies from transitions to excited states that are well above the initial onset of photofragmentation. Imaging allows one to compare the state-dependant intensities and branching ratios of each photoproduct channel, allowing one to investigate an analyte's dissociation dynamics and excited state structure far beyond the Franck-Condon region.<sup>8</sup> It can also be used to determine the rate of dissociation relative to the rotational period of the parent, yielding important information about the behavior of the excited state in question.

Photofragment imaging has been used to successfully explore the photodissociation and excited state dynamics of many interesting ions.<sup>9</sup> Although, for reasons that will be addressed later (Chapter 2), it has not yet been widely applied to the study of metal-containing ions. In Chapter 2, a new fast ion photofragment imaging mass spectrometer will be presented. This recently constructed instrument has been used to image the photofragments of a few challenging metal-containing ions. The spectroscopy and photofragment images of  $\text{N}_2\text{O}^+$  are compared to those of other current experimental<sup>10</sup>,<sup>11</sup> and theoretical<sup>12</sup> methods in order to assess the figures of merit of this new instrument. In Chapter 3, the photolysis of several excited states of the aluminum dimer cation ( $\text{Al}_2^+$ ) are investigated. In Chapter 4, the spectroscopy and dissociation dynamics of the theoretically challenging<sup>13, 14</sup> manganese oxide cation ( $\text{MnO}^+$ ) are addressed.

## 1.4 References

1. R. B. Metz, *Int. Rev. Phys. Chem.* **23**, 79-108 (2004).
2. A. Kocak, G. Austein-Miller, W. L. Pearson III, G. Altinay and R. B. Metz, *J. Phys. Chem. A* **117**, 1254-1264 (2013).
3. W. L. P. III, C. Copeland, A. Kocak, Z. Sallese and R. B. Metz, *J. Chem. Phys.* **141**, 204305 (2014).
4. D. J. Matthew, E. Tieu and M. D. Morse, *J. Chem. Phys.* **146**, 10 (2017).
5. A. Sevy, J. J. Sorensen, T. D. Persinger, J. A. Franchina, E. L. Johnson and M. D. Morse, *J. Chem. Phys.* **147**, 8 (2017).
6. D. R. A. Ranatunga and B. S. Freiser, *Chem. Phys. Lett.* **233**, 319-323 (1994).
7. D. W. Chandler and P. L. Houston, *J. Chem. Phys.* **87**, 1445-1447 (1987).
8. *Imaging in Chemical Dynamics*, edited by A. G. Suits and R. E. Continetti, ACS Symposium Series 770, (American Chemical Society, Washington DC, 2000).
9. M. N. R. Ashfold, N. H. Nahler, A. J. Orr-Ewing, O. P. J. Vieuxmaire, R. L. Toomes, T. N. Kitsopoulos, I. A. Garcia, D. A. Chestakov, S. M. Wu and D. H. Parker, *Phys. Chem. Chem. Phys.* **8**, 26-53 (2006).
10. H. Wang, X. Zhou, S. Liu, B. Jiang, D. Dai and X. Yang, *J. Chem. Phys.* **132**, 244309 (2010).
11. X. Tang, M. Niu, X. Zhou, S. Liu, F. Liu, X. Shan and L. Sheng, *J. Chem. Phys.* **134**, 054312 (2011).
12. G. Chambaud, H. Gritli, P. Rosmus, H. J. Werner and P. J. Knowles, *Mol. Phys.* **98**, 1793-1802 (2000).
13. C. W. Bauschlicher and G. L. Gutsev, *Theor. Chem. Acc.* **107**, 309-312 (2002).
14. E. Miliordos and A. Mavridis, *J. Phys. Chem. A* **114**, 8536-8572 (2010).

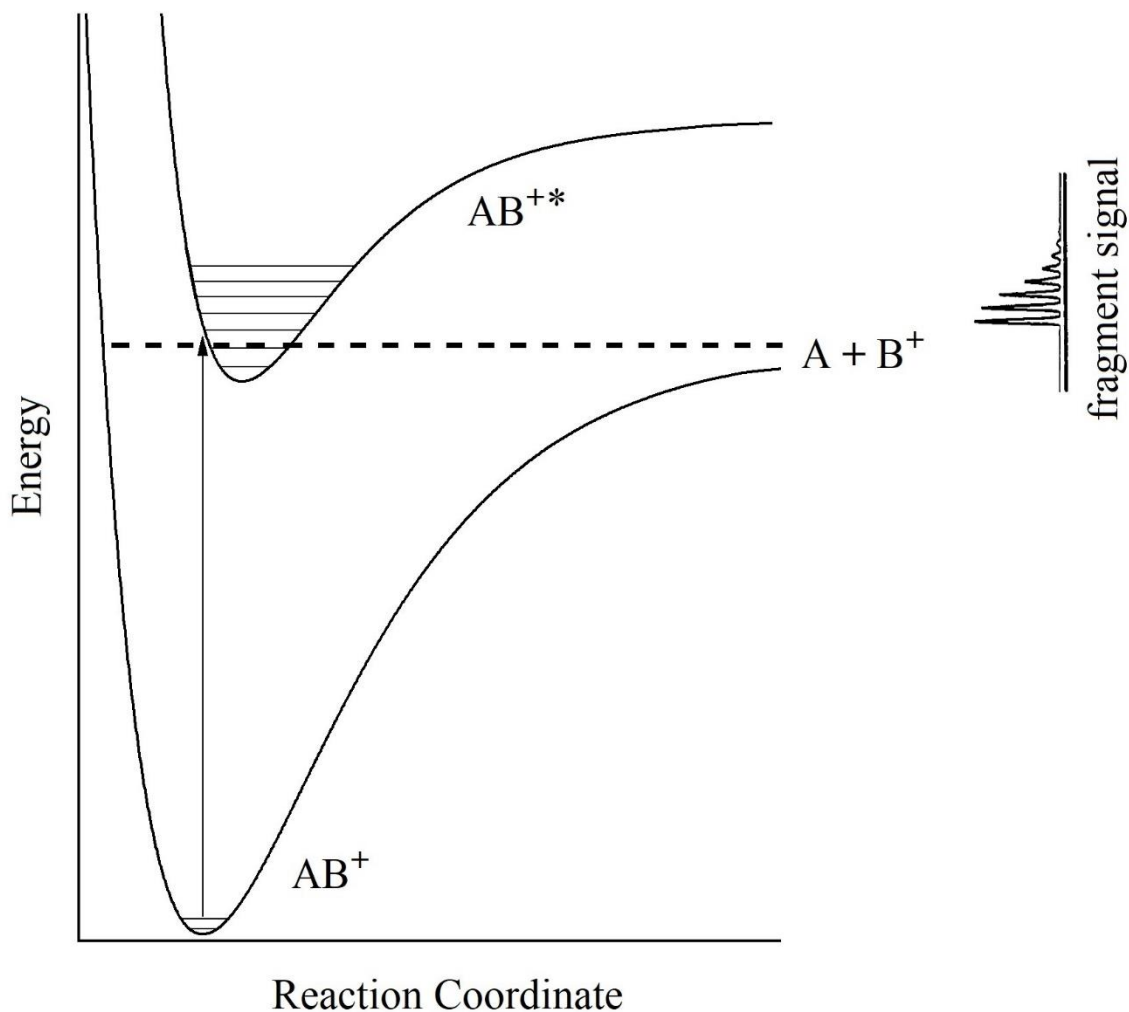


Figure 1.1. Potential energy surfaces depicting photon absorption by a cation ( $AB^+$ ) and the resulting photodissociation from an excited electronic state ( $AB^{+*}$ ) near the photoproduct ( $A + B^+$ ) threshold. The photon energy at the sudden onset of fragment signal is a good estimate for the bond dissociation energy.

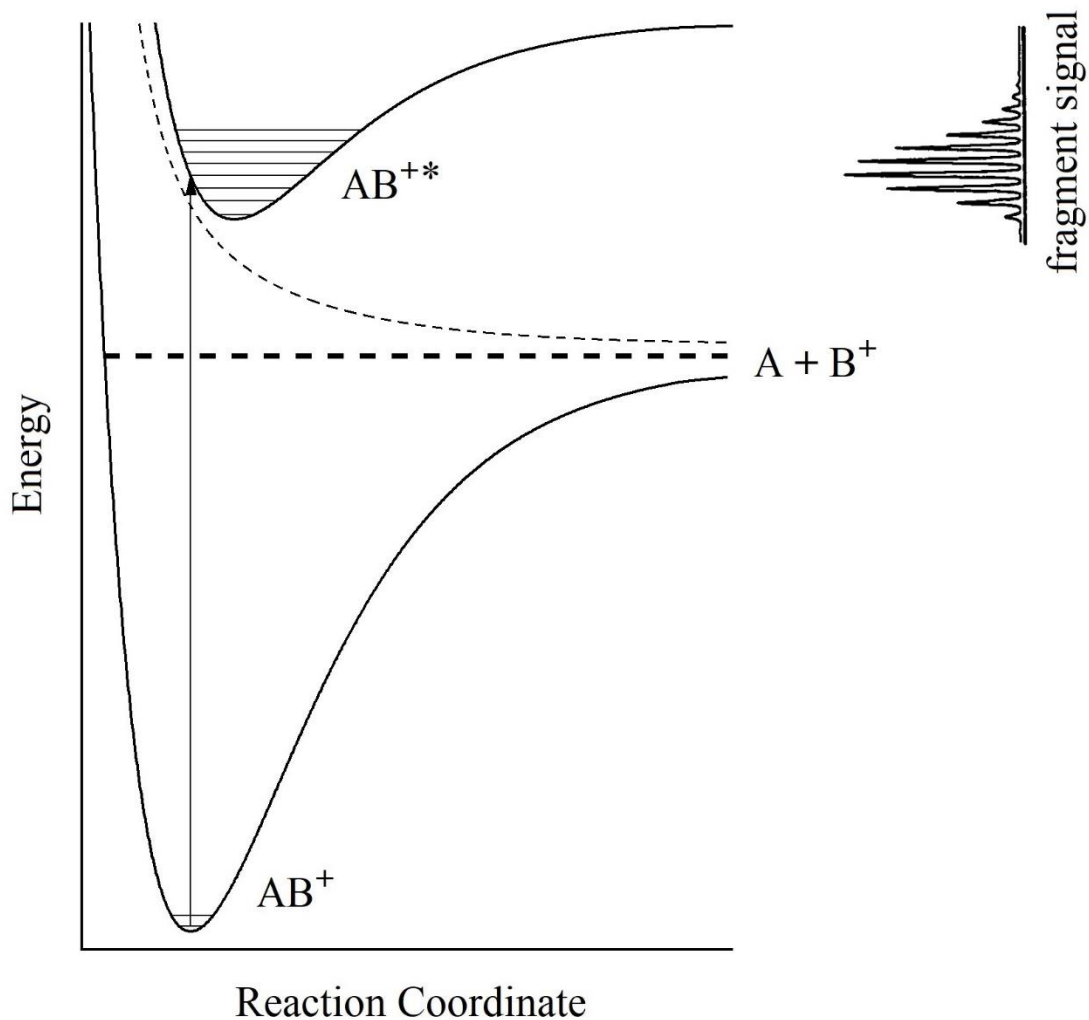


Figure 1.2. Potential energy surfaces depicting photon absorption by a cation ( $AB^+$ ) and the resulting predissociation from an excited electronic state ( $AB^{+*}$ ) well above the photoproduct ( $A + B^+$ ) threshold. The onset of fragment signal provides only an upper limit to the bond dissociation energy.

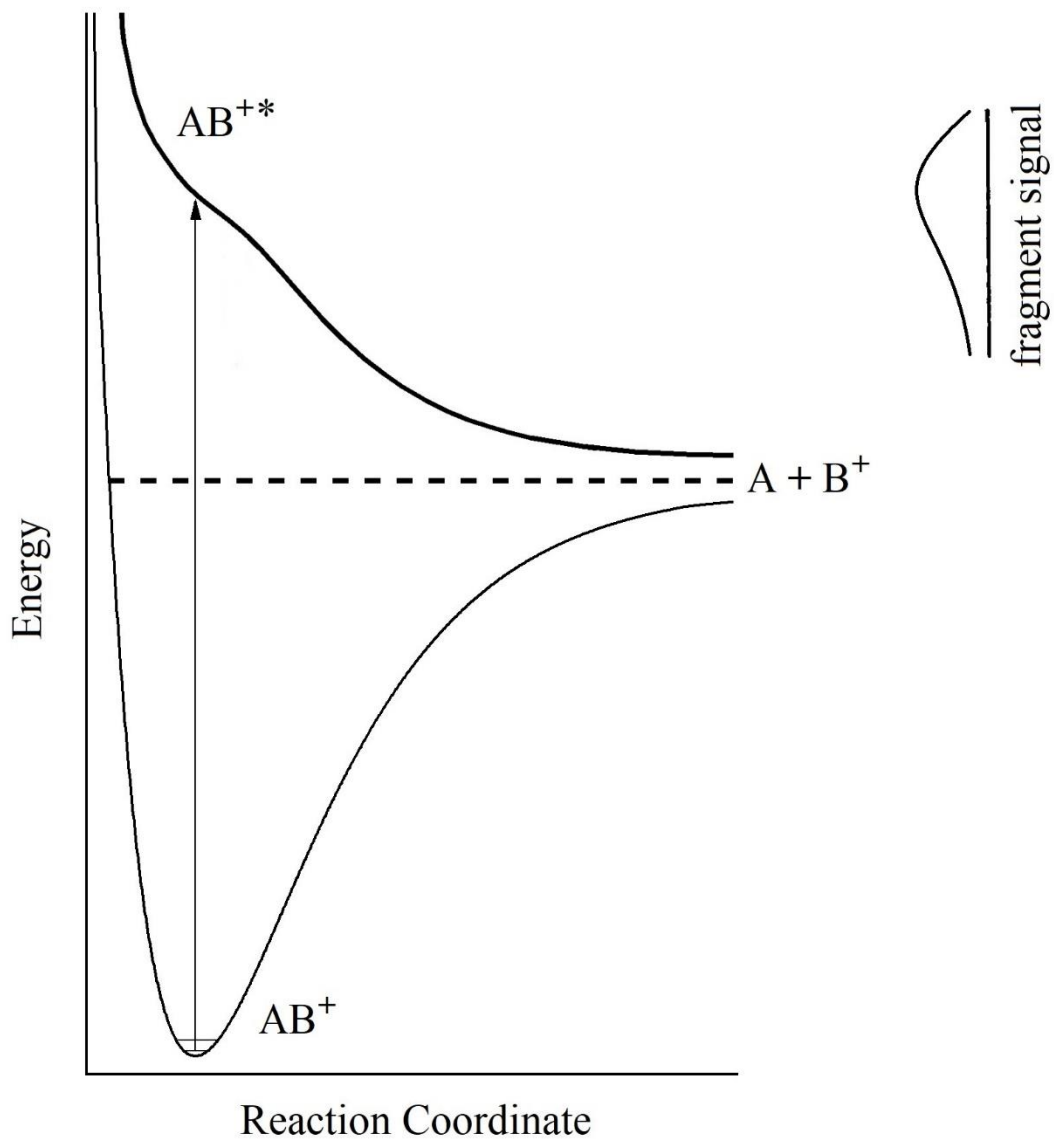


Figure 1.3. Potential energy surfaces depicting photon absorption by a cation ( $AB^+$ ) and the resulting photodissociation from a repulsive excited electronic state ( $AB^{+*}$ ) above the photoproduct ( $A + B^+$ ) threshold. The fragment signal is broad and unstructured, providing little information.

## CHAPTER 2

### EXPERIMENTAL

#### 2.1 Introduction

Ion imaging has been widely used in the study of photodissociation dynamics since the technique's inception in 1987.<sup>1</sup> The later advent of velocity map imaging (VMI) made it possible to measure the energetics and dynamics of bimolecular and unimolecular reactions with an unprecedented level of precision.<sup>2</sup> Subsequent imaging studies of photoinduced decomposition have been primarily focused on neutral molecules,<sup>3</sup> although several cases of ion photodissociation have been reported.<sup>4-16</sup> Further advancements in electronics, detection methods,<sup>17-20</sup> and image processing routines<sup>21-23</sup> have increased the variety of molecules studied and the quality of data being produced by the imaging community.<sup>24, 25</sup>

Imaging experiments aimed at studying the unimolecular decomposition of *ions* typically employ resonance enhanced multiphoton ionization (REMPI) to state-selectively prepare the species of interest in a molecular beam. After photolysis, the fragment ions are projected onto a two-dimensional detector via a series of velocity mapping optics in order to precisely measure their angular distributions and kinetic energy release (KER). Many interesting ions have been investigated with some variant of this arrangement. However, there are countless others that are excluded by it, mainly due to the selectivity and low yield of the ionization scheme. More specifically, ions that do not have stable neutral precursors with suitable intermediate electronic states cannot be prepared by REMPI. With laser ablation, pulsed discharge, and electrospray sources, the greater resolution of state selective methods is lost in exchange for greater versatility and

signal, allowing informative photofragment imaging experiments to be performed on a host of ions that would otherwise be inaccessible. For example, the photofragments of  $\text{Ar}_2^+$  and  $\text{Ag}^+(\text{benzene})$  have recently been imaged on a VMI instrument that employs a laser ablation/spark source.<sup>14, 15</sup> In this chapter, we demonstrate a new instrument that is capable of velocity map imaging the mass selected photofragments of trap-cooled ions produced in a variety of ion sources.

It is worth noting that the maximum attainable resolution in these fragment imaging experiments is expected to be lower than techniques that image photoelectrons.<sup>26, 27</sup> The challenges associated with detecting atomic and molecular photoproducts are a consequence of their comparatively high mass. A less massive product, like an electron, will depart with greater velocity at a given KER, resulting in a significantly reduced kinetic energy per pixel term and far less dependence on the position and velocity spread of the parent.

The experimental scheme described here is the result of a series of augmentations that have been made to a previously built<sup>28</sup> reflectron time-of-flight apparatus. The new instrument is capable of performing photodissociation spectroscopy and velocity map imaging experiments on fast ion beams. The ions are created by a dual-mode ion source and cooled in a refrigerated 3D Paul trap. Photofragment images of  $\text{N}_2\text{O}^+$  dissociated in the UV are presented and analyzed in the later sections in order to demonstrate the capabilities and initial resolution of the fast ion photofragment imaging mass spectrometer.

## 2.2 Instrumental

The main components of the instrument (Figure 2.1) are housed in three differentially pumped vacuum chambers and are described in detail in the following sections. Ions are generated in the source region before being sent to the trap chamber via a quadrupole ion guide. Once extracted from the trap, the ions are accelerated into the final region where they are spectroscopically interrogated. The instrument has two modes of operation corresponding to two different flight paths, one for photodissociation spectroscopy and the other for photofragment imaging. In both modes, the analytes are selected based on their mass to charge ratio in a traditional time-of-flight approach. Photodissociation spectroscopy is performed by photolyzing the ions at the turning point of the reflectron and monitoring the photofragments at the corresponding microchannel plate (MCP) detector (path 1). Imaging studies are conducted by grounding the reflectron and sending the beam through an offset deflector and iris, to the velocity mapping optics and imaging detector (path 2).

### 2.2.1 Ion Source

The multipurpose ion source (Figure 2.2) is designed to switch between laser ablation and pulsed discharge ionization modes as needed without venting the chamber. The source may also be outfitted with a separate customized electrospray attachment.<sup>28</sup> Metal-containing cations are formed by focusing the second harmonic output of a Continuum Minilite II ( $\leq 20$  mJ/pulse, 500  $\mu\text{m}$  dia. spot) onto a rotating disc of the desired metal.<sup>29</sup> The metal disc can usually be ablated for  $\sim 20$  hours ( $\sim 1.3$  million shots) before it must be polished to improve parent generation. A reactant/carrier gas mix at 20-

60 psi backing pressure is pulsed at 18 Hz by a solenoid valve (Parker, series 9) into the ablation block where it intercepts the recently formed plume of hot ablation products. The metal ions in the plume collide with the carrier gas in a narrow channel (2.5 mm dia.) over a distance of 13 mm before experiencing a supersonic expansion into the vacuum chamber.

In order to directly ionize a gaseous precursor, the source can be toggled into high voltage pulsed discharge mode. In this setup, a pulse of up to 2.0 kV is applied to a thin wire at the exit of the ablation block just as the gas pulse begins its expansion into vacuum. Current is conducted through the expanding gas to the grounded wire on the opposite side of the outlet, ionizing the analyte in the process. Once the target ions have expanded into vacuum, they are immediately focused through an aperture lens (9 mm dia.) into the quadrupole ion guide (190 V pk-pk at 2.8 MHz),<sup>30</sup> which delivers them to the trap. A source pressure of  $10^{-2}$  Torr is maintained by a large mechanical pump (Alcatel 2060C). The quadrupole chamber bridges the source and trap chambers and is evacuated by a turbo molecular pump (Edwards EXT255) backed by a mechanical pump (Leybold Trivac D65B).

### **2.2.2 Ion Trap**

In an imaging experiment, a precise measurement of bond dissociation energy ( $D_0$ ) comes from applying conservation of energy along with careful accounting. It is therefore crucial to start with a parent beam whose internal energy is both minimal and well defined. Unfortunately, difficulty in achieving this end can arise from the use of laser ablation or HV discharge sources. Such hard ionization techniques tend to generate

ions in excited vibrational and electronic states that cannot be effectively cooled to an equilibrium distribution by an adiabatic expansion into vacuum. In light of this, a cold trapping scheme has been added. In addition to being a more tractable method of bringing ions to a user-defined equilibrium temperature, trapping has the added benefit of improving signal and signal stability. Collecting an ion packet over the entire experimental cycle prior to extraction tends to smooth out any signal fluctuations that would otherwise arise from shot to shot timing inconsistencies in the source. This also makes it possible to image cold ions in large quantities even if they originate from a continuous source like electrospray.

The execution of our cold trapping strategy (Figure 2.3) is similar to those reported by Wang *et al.*<sup>31</sup> and Kamrath *et al.*<sup>32</sup> A 3D Paul trap (R. M. Jordan) is attached to the second stage ( $\geq 7\text{K}$ ) of a closed cycle helium refrigerator (cold head: Sumitomo CH-204 SFF-N; compressor: Sumitomo HC-4A). A heater cartridge is used to maintain the desired temperature, which is measured by a silicon diode (DT-670B) on the second stage that is read by a digital controller (Lakeshore 335). The trap itself is mounted onto the cold head through a custom adapter made from an oxygen free high conductivity copper block, a thin sapphire plate (1 mm), and several sheets of indium foil. This arrangement provides excellent thermal conductivity between the trap and the cold head while also electrically isolating the trap electrodes from the refrigerator. The trap is enclosed in custom-made aluminum “can” that is fastened to the first stage ( $\geq 40\text{K}$ ) of the refrigerator. The can acts as a thermal radiation shield by limiting direct line-of-sight to the trap from external black body emitters. The entire assembly is mounted onto an adjustable bellows for alignment.

To accommodate the new can and refrigerator, the trap was repositioned to the center of the chamber, necessitating a complete overhaul of the ion guide scheme. The old double octupole has been replaced by a single 330 mm long quadrupole, which improves the overall ion signal by filling the trap more effectively. A cross section of the occupiable volume in a quadrupole is smaller than that of an octupole, so the ions leave the quadrupole in a tighter packet. Once the ions exit the ion guide, they are focused into the trap by a set of aperture and tube lenses that are affixed to the trap's thermal shielding and end caps respectively. An RF signal with variable frequency and amplitude ( $\leq 500$  V pk-pk at 400 - 800 kHz) is applied to the central ring of the trap by a circuit based on the driver described by Jau *et al.*<sup>33</sup>

Ions are held in the trap and allowed to collisionally thermalize with a cooled buffer gas, which is introduced by a pulsed valve (Parker, series 9) affixed to the bottom of the thermal shield. The pulsed valve and several metallic tube fittings are in thermal contact with the shield, increasing the potential of leaks due to daily thermal contraction and expansion. To counteract this, a Teflon poppet, which maintains some plasticity at very cold temperatures, is used. Teflon tape is also used to bind the affected ferrules and tube fittings, effectively filling the small gaps that may form at the metal/metal junctions. The trapping time is typically set to 50 ms to maximize the number of buffer gas collisions and minimize the amount of residual gas left in the chamber upon extraction. Ions enter the trap for  $\sim 3$  ms when the local buffer gas pressure is at its highest. The low temperatures achieved in the trap necessitate the use of buffer gases with sufficiently high vapor pressures. Hydrogen (either pure or mixed with He) is typically used because it has a larger collisional cross section and quenching efficiency than helium. Pure helium is

typically used if the analyte reacts with hydrogen, as is the case with  $\text{N}_2\text{O}^+$  and  $\text{MnO}^+$ . Oxygen may also be included in the buffer gas mix if it is suspected that low-lying excited electronic states are populated.

Ions are extracted at 18 Hz in a Wiley-McLaren configuration by a pulsed bipolar voltage applied to the end caps of the trap. A bipolar extraction ensures that the field lines seen by the ion packet at the center of the trap are even, thus helping to prevent a divergent beam.<sup>34</sup> The extraction pulse is timed to occur at a zero crossing of the RF voltage. Upon leaving the trap, the ions encounter a mirrored set of aperture and tube lenses, which collimate the beam as it approaches the nearby acceleration region. The trap chamber and the adjacent acceleration region are held at  $10^{-6}$  Torr by two diffusion pumps (Edwards Diffstak 160), each backed by a mechanical pump (Leybold Trivac D8B).

### **2.2.3 Beam Acceleration and Manipulation**

The ion beam is accelerated by -1800 V DC, which is applied to a short section of the flight tube (110 mm long, 6.4 mm dia.). In order to avoid floating the instrument at high voltage, the accelerated ions are re-referenced to ground potential.<sup>35</sup> The ions enter a re-referencing tube maintained at -1800 V until such time as the ion packet is fully inside, when it is summarily pulsed<sup>36</sup> to ground. The ion beam is then steered and collimated by a series of DC deflectors and Einzel lenses. A small opening (10 mm dia.) separates the trap/acceleration region from the detection chamber, which is kept at  $10^{-7}$  Torr by two turbo pumps (Pfeiffer TMU260, Leybold Turbovac 361) backed by a mechanical pump (Varian SD-450). A pulsed horizontal deflector is used to guide the target ions either to

the reflectron or to the velocity map imaging optics. This deflector also serves as a mass gate to prevent cluttering of the mass spectrum at the detector. If photodissociation spectroscopy is to be performed, the parent ions are directed into a gridless reflectron, where they are irradiated by the photolysis laser at the turning point (path 1 in Figure 2.1). The photofragments have a characteristic flight time to the detector; it is distinct from that of the remaining parents' due to reacceleration by the reflectron.

In order to image the photofragments, a movable stage holding a horizontal deflector and an adjustable iris is manually raised into the path of the ion beam (path 2 in Figure 2.1). The horizontal deflector is set to correct for the bend in the ion beam imposed by the mass gate and to ensure that the beam is coaxial with the velocity mapping optics as it passes through the grounded reflectron. The diameter of the iris (1-12 mm) is adjusted in vacuum by a linear actuator (Firgelli PQ12) and the accompanying software. Passing the ion beam through the small apertures in the iris and in the front VMI plate (0.7 meters apart) minimizes contribution to the fragment transverse velocity from the original beam divergence, thereby improving image resolution. While it is possible to do photodissociation spectroscopy studies at the imaging detector, the aforementioned apertures greatly reduce the overall signal in comparison to the relatively unrestricted flight path to the reflectron detector.

#### **2.2.4 Velocity Map Imaging**

After the ion packet has been radially constricted by the iris, it enters the velocity map imaging apparatus (Figure 2.4). The VMI stack consists of three electrically isolated ion optics spaced by 15 mm. The stack is mounted onto four glass-insulated stainless

steel posts attached to a flange inside the flight tube. Each optic is a 1.65 mm thick, 90.7 mm diameter steel disc with a hole drilled in the center. The first VMI ion optic ( $IO_1$ ) has a narrow aperture (3 mm dia.); the openings in the final two are larger (20 mm dia.). As soon as the ion packet has passed through  $IO_1$  (2.14 m from the center of the ion trap), it is crossed by the vertically polarized output of a pulsed dye laser (Continuum ND6000) pumped by the second or third harmonic of a Nd:YAG (Continuum Powerlite 8020), causing some of the ions to dissociate. Concurrently,  $IO_1$  and  $IO_2$  are charged with separate high voltage pulses (DEI PVM4150), while  $IO_3$  remains grounded. The resulting field acts as an electrostatic lens (Figure 2.4), reaccelerating and focusing the expanding fragment cloud onto the imaging detector (1 meter away). The voltages are determined by simulating ion flight paths in the SIMION software package<sup>37</sup> and later adjusting for improved resolution at the imaging detector. A voltage ratio ( $IO_1/IO_2$ ) between 1.02 and 1.10 is typical.

Optimized VMI voltages allow fragments with different points of origin to arrive at the same radius on the detector as long as they have the same transverse velocity.<sup>2</sup> In typical imaging experiments, the initial speed of the parents is negligible compared to the velocity gained by reacceleration. However, in a fast ion beam, the original beam speed is often greater than the secondary velocity gain due to VMI. This key difference means that the exact voltages being applied to the imaging optics are somewhat dependent on the mass of the analyte and that the process of simulating and carefully optimizing ion optics voltages must be undertaken for each new  $m/z$ . On the positive side, and for much the same reason, the cloud of fast ion photofragments is hardly magnified at all by the VMI lens.

The imaging detector (Photonis) consists of two MCPs (120 mm dia., 25  $\mu\text{m}$  pore, 32  $\mu\text{m}$  pitch, 2 mm thick, 8° bias) in a chevron configuration coupled to a fast phosphor screen (P47) operating at 4.0 kV. The back MCP is kept at a DC level of -1.5 kV while the front plate is pulsed from ground up to +700 V for 200-700 ns, creating a voltage difference of 2.2 kV between the plates that coincides with the arrival of the whole fragment cloud. The large capacitance of our MCPs does not allow for a detector pulse that is narrow enough to slice<sup>15, 17</sup> a fragment cloud with ~3 keV of kinetic energy. Therefore, the entire cloud must be mathematically reconstructed after acquisition. The difference in time-of-flight between the reaccelerated fragments and the remaining parents is 0.6  $\mu\text{s}$  ( $\text{NO}^+/\text{N}_2\text{O}^+$ ), sufficient to discriminate against any residual parent signal in the images. Gating the MCPs narrowly on the fragment signal also allows one to reject any stray ions with similar arrival times and any dark current background that could otherwise accumulate over many cycles.

### **2.2.5 Data Acquisition and Processing**

The rear of the fast phosphor screen is monitored by a photomultiplier tube (PMT) synced to a digital oscilloscope. Composite photofragment images are captured by a CCD camera (IDS  $\mu\text{Eye}$ , 1024 x 768 pixels) and compiled on a desktop computer using NuAcq software.<sup>20</sup> The high sensitivity of the PMT allows the discriminated parent signal to continue to be monitored despite being too weak to be seen by the camera. All precision timings are controlled by a set of digital delay generators (Stanford Research DG535). Image reconstruction is done by inverse Abel transform using the BASEX

method, the advantages of which have been discussed elsewhere in detail.<sup>21</sup> Images are typically averaged over 20,000 to 100,000 laser shots.

The bond dissociation energy ( $D_0$ ) of an ion can be found by measuring the radial distribution of photofragments in an image and using the corresponding transverse velocity distribution to derive the total kinetic energy release. Careful energy accounting is the key to a precise determination of  $D_0$ . For a non-radiative photodissociation process, the following is true by conservation of energy:

$$E_{\text{Parent}} + h\nu = D_0 + E_{\text{Frag}} + E_{\text{Cofrag}} + \text{KER}_{\text{total}} \quad (2.1)$$

If the parent's internal energy ( $E_{\text{Parent}}$ ) is well defined, and the populated internal states of the detected fragment ( $E_{\text{Frag}}$ ) and cofragment ( $E_{\text{Cofrag}}$ ) are sufficiently separated and identified, one can measure  $\text{KER}_{\text{total}}$  from an image's radius at a particular photolysis energy ( $h\nu$ ) to find a precise value of  $D_0$ . The resolution of a given image can then be defined as the FWHM of its velocity distribution ( $\Delta v$ ) divided by the most probable velocity ( $v$ ). The exact value can vary between images of the same analyte because it is highly dependent upon instrumental variables like VMI voltages, VMI pulse timing, and ion/laser overlap. The highest resolution we have achieved ( $\Delta v / v = 7.6\%$ ) is obtained from the images of  $\text{Al}_2^+$  fragments, which are discussed in Chapter 3.

Anisotropy in the photofragment image of a linear molecule is dependent upon three factors: the orientation of the principal molecular axis relative to the direction of the photolysis laser polarization, the orientation of the relevant transition dipole moment, and the excited molecule's dissociative lifetime. For dissociative events that occur faster than the parent's rotational period, a parallel transition yields a photofragment image with greater intensity along the axis that is parallel to the laser polarization vector. Likewise,

excitation of a perpendicular transition produces an image with intensity along the axis perpendicular to that of the polarization vector. The intensity distribution of an image is fit to the following equation:

$$I(\theta) = \frac{A}{4\pi} [1 + \beta P_2(\cos(\theta))] \quad (2.2)$$

where  $\theta$  is the angle between the laser polarization vector and a given radial position on the image.  $P_2(\cos(\theta))$  is the second order Legendre polynomial. The value of the anisotropy parameter ( $\beta$ ) ranges from -1 to 2 for images showing the limiting cases of purely perpendicular or parallel character, respectively. A value of 0 represents a totally isotropic image for which any information regarding the orientation of the transition dipole moment has been lost. Radial distribution isotropy usually arises from long lived predissociative processes but in some cases, it could be due to an unresolved mixing of excited state symmetry in the parent.

### 2.3 Preliminary Results: $\text{N}_2\text{O}^+$

In order to evaluate the merits of the new instrument,  $\text{N}_2\text{O}^+$  has been prepared by electric discharge and images of  $\text{NO}^+$  photoproducts resulting from the bound to bound  $^2\Sigma^+ \leftarrow ^2\Pi$  transition are reported here and discussed in relation to the current literature.  $\text{N}_2\text{O}^+$  is made by pulsing a precursor gas mix (10%  $\text{N}_2\text{O}$  in He) at 20 psi backing pressure into the source chamber operating in pulsed electric discharge mode. It was identified as an early candidate for fast ion imaging because its excited state dynamics have been studied extensively by theory,<sup>38</sup> spectroscopy,<sup>39-43</sup> and imaging.<sup>11, 44</sup> The  $D_0$  of  $\text{N}_2\text{O}^+$  is well known ( $10,430 \pm 160 \text{ cm}^{-1}$ ),<sup>45</sup> so it can be used along with the image radii to evaluate the spatial resolution of the imaging camera (0.074 mm/pixel). The  $^2\Sigma^+$  excited

state of  $\text{N}_2\text{O}^+$  predissociates, and the rotationally resolved electronic spectrum has long progressions and combinations of all three vibrations. When dissociated in the UV,  $\text{N}_2\text{O}^+$  shows interesting product state branching tendencies. Only the ground state product channel ( $\text{N}(^4\text{S}) + \text{NO}^+$ ) is energetically accessible from the  $^2\Sigma^+(200) \leftarrow ^2\Pi_{3/2}(000)$  transition at  $\sim 323$  nm ( $30,914$   $\text{cm}^{-1}$ ). It appears as a wide isotropic distribution centered at  $\sim 9000$   $\text{cm}^{-1}$  total KER (Figure 2.5 top), indicating that the  $\text{NO}^+$  is produced almost exclusively in a specific vibrational state ( $v=5$ ) with a large degree of unresolved rotational excitation. The unusually wide peak is evidence that many excited rotational levels are populated and are contributing to the spread of possible fragment velocities. The presence of these rotationally hot products can be attributed to the bent geometry of a  $^4\Pi$  potential energy surface in the parent that the  $^2\Sigma^+$  excited state must ultimately couple to via spin-orbit interactions during the dissociative process.<sup>11, 38</sup> A transition to the next quantum of symmetric stretch,  $^2\Sigma^+(300) \leftarrow ^2\Pi_{3/2}(000)$  at  $\sim 310$  nm ( $32,238$   $\text{cm}^{-1}$ ), is energetic enough to access an electronically excited product channel,  $\text{N}^*(^2\text{D}) + \text{NO}^+$ . This new spin-allowed pathway, manifested by the intense inner rings (Figure 2.5 bottom), is favored over lower energy (spin-forbidden) product formation. The slight perpendicular anisotropy ( $\beta = -0.31$ ) seen in the intermediate ring may indicate that some of the perpendicular character of the ( $^2\Sigma^+ \leftarrow ^2\Pi$ ) transition isn't fully lost in the predissociative process. Both the channel switching effect seen at 310 nm, and the vibrational population inversion seen in the products after dissociation at 323 nm are consistent with previous studies.<sup>11, 40, 41, 43, 44</sup>

## 2.4 Conclusions

In summary, we demonstrate an instrument that is capable of performing velocity map imaging (VMI) on the photofragments of cold, mass selected ions in a fast ion beam. The ions are produced in a dual laser ablation/discharge source and collisionally thermalized in a refrigerated ( $\geq 7$  K) ion trap prior to spectroscopy and imaging. The current limiting resolution of the experiment ( $\Delta v / v = 7.6\%$ ) and the factors that contribute to it have been determined by analyzing the radial distributions of several photolysis products. Preliminary images of  $\text{N}_2\text{O}^+$  support the finding that photodestruction at 323 nm yields rotationally hot  $\text{NO}^+$  fragments primarily in  $v=5$ . Images of  $\text{N}_2\text{O}^+$  photolysis at 310 nm reveal the expected competition between spin-forbidden ground state product formation ( $\text{N}(^4\text{S}) + \text{NO}^+$ ) and a spin-allowed excited state product channel ( $\text{N}^*(^2\text{D}) + \text{NO}^+$ ), which is consistent with the published literature. In Chapters 3 and 4, this instrument will be used to measure the kinetic energy release and anisotropy in photofragments of  $\text{Al}_2^+$  and  $\text{MnO}^+$ .

## 2.5 References

1. D. W. Chandler and P. L. Houston, *J. Chem. Phys.* **87**, 1445-1447 (1987).
2. A. T. J. B. Eppink and D. H. Parker, *Rev. Sci. Instrum.* **68**, 3477-3484 (1997).
3. M. N. R. Ashfold, N. H. Nahler, A. J. Orr-Ewing, O. P. J. Vieuxmaire, R. L. Toomes, T. N. Kitsopoulos, I. A. Garcia, D. A. Chestakov, S. M. Wu and D. H. Parker, *Phys. Chem. Chem. Phys.* **8**, 26-53 (2006).
4. M. Beckert, S. J. Greaves and M. N. R. Ashfold, *Phys. Chem. Chem. Phys.* **5**, 308-314 (2003).
5. N. H. Nahler, O. P. J. Vieuxmaire, J. R. Jones, M. N. R. Ashfold, A. T. J. B. Eppink, A. M. Coriou and D. H. Parker, *J. Phys. Chem. A* **108**, 8077-8083 (2004).
6. M. H. Kim, B. D. Leskiw and A. G. Suits, *J. Phys. Chem. A* **109**, 7839-7842 (2005).
7. A. D. Webb, R. N. Dixon and M. N. R. Ashfold, *J. Chem. Phys.* **127**, 224307 (2007).
8. A. D. Webb, N. H. Nahler and M. N. R. Ashfold, *J. Phys. Chem. A* **113**, 3773-3778 (2009).
9. A. G. Sage, T. A. A. Oliver, R. N. Dixon and M. N. R. Ashfold, *Mol. Phys.* **108**, 945-955 (2010).
10. P. C. Singh, L. Shen, J. Zhou, H. B. Schlegel and A. G. Suits, *Astrophys. J.* **710**, 112-116 (2010).
11. H. Wang, X. Zhou, S. Liu, B. Jiang, D. Dai and X. Yang, *J. Chem. Phys.* **132**, 244309 (2010).
12. H. L. Tao, L. Shen, M. H. Kim, A. G. Suits and T. J. Martinez, *J. Chem. Phys.* **134**, 054313 (2011).
13. I. S. Parry, A. C. Hermes, A. Kartouzian and S. R. Mackenzie, *Phys. Chem. Chem. Phys.* **16**, 458-466 (2014).
14. J. A. Maner, D. T. Mauney and M. A. Duncan, *J. Phys. Chem. Lett.* **6**, 4493-4498 (2015).
15. J. A. Maner, D. T. Mauney and M. A. Duncan, *Chem. Phys. Lett.* **671**, 182-185 (2017).

16. K. Okutsu, Y. Nakashima, K. Yamazaki, K. Fujimoto, M. Nakano, K. Ohshimo and F. Misaizu, *Rev. Sci. Instrum.* **88**, 053105 (2017).
17. D. Townsend, M. P. Minitti and A. G. Suits, *Rev. Sci. Instrum.* **74**, 2530-2539 (2003).
18. B. Y. Chang, R. C. Hoetzlein, J. A. Mueller, J. D. Geiser and P. L. Houston, *Rev. Sci. Instrum.* **69**, 1665-1670 (1998).
19. C. R. Gebhardt, T. P. Rakitzis, P. C. Samartzis, V. Ladopoulos and T. N. Kitsopoulos, *Rev. Sci. Instrum.* **72**, 3848-3853 (2001).
20. W. Li, S. D. Chambreau, S. A. Lahankar and A. G. Suits, *Rev. Sci. Instrum.* **76**, 063106 (2005).
21. V. Dribinski, A. Ossadtchi, V. A. Mandelshtam and H. Reisler, *Rev. Sci. Instrum.* **73**, 2634-2642 (2002).
22. G. A. Garcia, L. Nahon and I. Powis, *Rev. Sci. Instrum.* **75**, 4989-4996 (2004).
23. S. Manzhos and H.-P. Looock, *Comput. Phys. Commun.* **154**, 76-87 (2003).
24. *Imaging in Chemical Dynamics*, edited by A. G. Suits and R. E. Continetti, ACS Symposium Series 770, (American Chemical Society, Washington DC, 2000).
25. *Imaging in Molecular Dynamics: Technology and Applications*, edited by B. J. Whitaker, (Cambridge University Press, New York, 2003).
26. D. M. Neumark, *J. Phys. Chem. A* **112**, 13287-13301 (2008).
27. A. Sanov and R. Mabbs, *Int. Rev. Phys. Chem.* **27**, 53-85 (2008).
28. R. B. Metz, *Int. J. Mass Spectrom.* **235**, 131-143 (2004).
29. S. E. Waller, J. E. Mann and C. C. Jarrold, *J. Phys. Chem. A* **117**, 1765-1772 (2013).
30. R. M. Jones, D. Gerlich and S. L. Anderson, *Rev. Sci. Instrum.* **68**, 3357-3362 (1997).
31. X. B. Wang and L. S. Wang, *Rev. Sci. Instrum.* **79**, 073108 (2008).
32. M. Z. Kamrath, R. A. Relph, T. L. Guasco, C. M. Leavitt and M. A. Johnson, *Int. J. Mass Spectrom.* **300**, 91-98 (2011).

33. Y. Y. Jau, F. M. Benito, H. Partner and P. D. D. Schwindt, *Rev. Sci. Instrum.* **82**, 023118 (2011).
34. B. B. Dangi and K. M. Ervin, *J. Mass Spectrom.* **47**, 41-48 (2012).
35. L. A. Posey, M. J. DeLuca and M. A. Johnson, *Chem. Phys. Lett.* **131**, 170-174 (1986).
36. R. E. Continetti, D. R. Cyr and D. M. Neumark, *Rev. Sci. Instrum.* **63**, 1840-1841 (1992).
37. D. A. Dahl, *Int. J. Mass Spectrom.* **200**, 3-25 (2000).
38. G. Chambaud, H. Gritli, P. Rosmus, H. J. Werner and P. J. Knowles, *Mol. Phys.* **98**, 1793-1802 (2000).
39. S. Abed, M. Broyer, M. Carre, M. L. Gaillard and M. Larzilliere, *Chem. Phys.* **74**, 97-112 (1983).
40. J. Lerme, S. Abed, M. Larzilliere, R. A. Holt and M. Carre, *J. Chem. Phys.* **84**, 2167-2179 (1986).
41. M. Richardviard, O. Atabek, O. Dutuit and P. M. Guyon, *J. Chem. Phys.* **93**, 8881-8892 (1990).
42. H. Xu, Y. Guo, S. Liu, X. Ma, J. Liang and H. Li, *J. Chem. Phys.* **119**, 11609-11614 (2003).
43. H. Xu, Y. Guo, Q. Li, Y. Shi, S. Liu and X. Ma, *J. Chem. Phys.* **121**, 3069-3073 (2004).
44. X. Tang, M. Niu, X. Zhou, S. Liu, F. Liu, X. Shan and L. Sheng, *J. Chem. Phys.* **134**, 054312 (2011).
45. J. H. Callomon and F. Creutzberg, *Philos. Trans. Roy. Soc. London, Ser. A* **277**, 158-189 (1974).

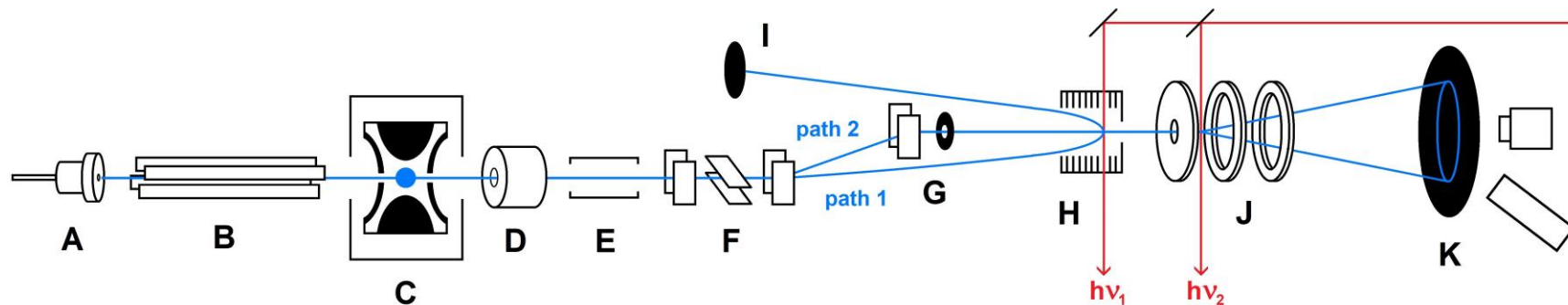


Figure 2.1. Schematic overview of the fast ion photofragment imaging mass spectrometer. Ions are produced in the source (A) and carried by an RF quadrupole (B) into the refrigerated ion trap (C). After extraction, ions are accelerated (D) and re-referenced to ground potential (E). A series of horizontal and vertical deflectors (F) guides the ion beam along the desired path. For photodissociation spectroscopy (path 1,  $h\nu_1$ ), the reflectron (H) sends photofragments to the first MCP detector (I). For photofragment imaging (path 2,  $h\nu_2$ ), a mass gate and adjustable iris (G) straighten the beam through to the VMI optics (J). Fragments are projected onto the imaging detector (K) and observed by a PMT and CCD camera. Sizes and distances are not to scale.

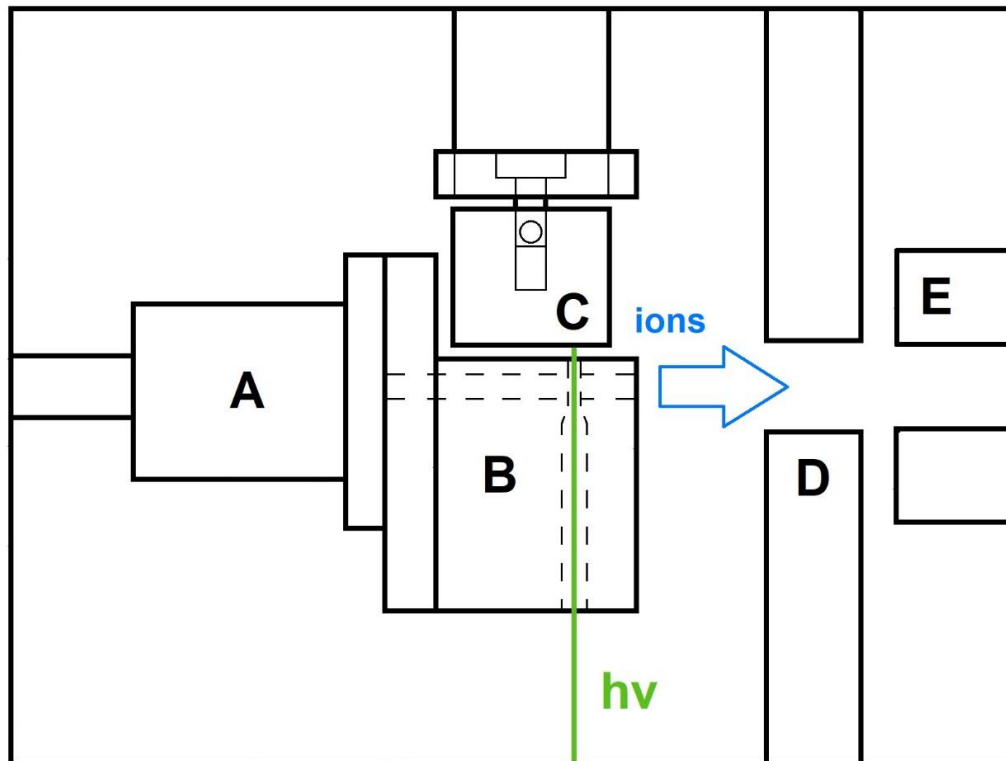


Figure 2.2. Detail of the ion source in laser ablation mode (top view). The carrier gas is introduced by a pulsed valve (A) into the ablation block (B), where it entrains the ions being ablated from the metal disc (C). Ions expanding into vacuum are focused by an aperture lens (D) into the RF quadrupole (E).

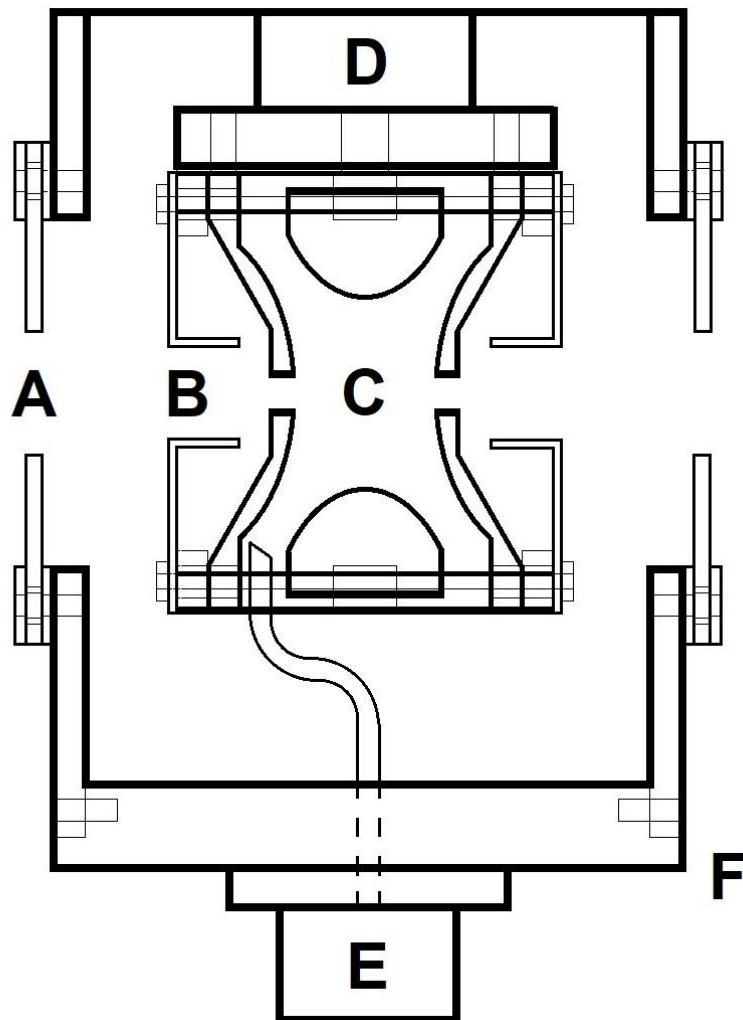


Figure 2.3. Detail of the refrigerated ion trap assembly. Ions are focused by a mirrored pair of aperture lenses (A) and tube lenses (B) into and out of the 3D Paul trap (C). The trap is coupled to the second stage of the refrigerator by a copper adapter (D). A pulsed valve (E) affixed to the aluminum “can” (F) introduces cold buffer gas to the center of the trap.

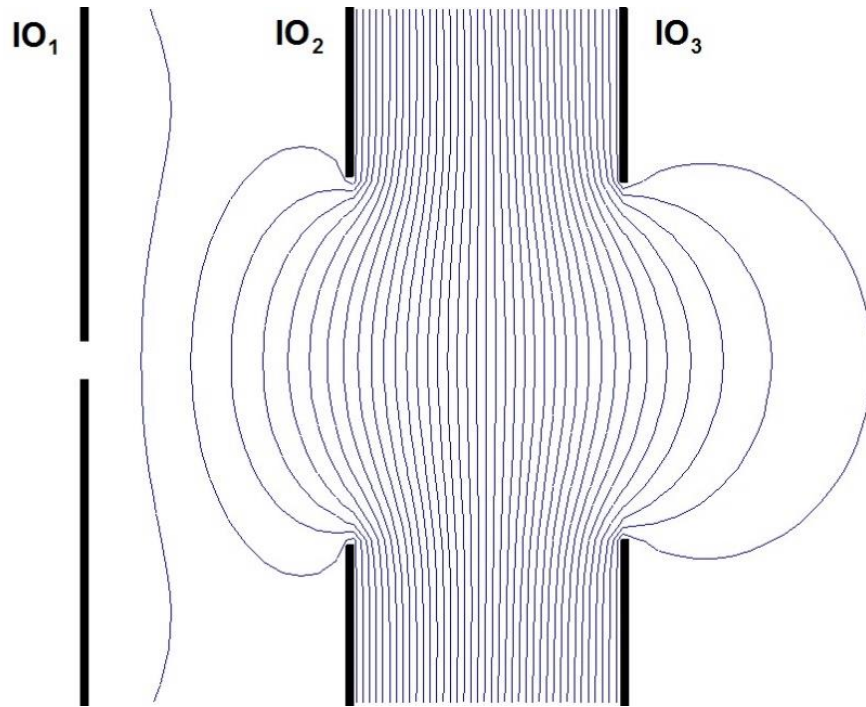


Figure 2.4. Detail of the velocity map imaging ion optics (IO) showing the equipotential lines at 30 V intervals for optimized Al<sub>2</sub><sup>+</sup> settings (Generated using SIMION 7.0). IO<sub>1</sub>= +1230 V, IO<sub>2</sub>= +1200 V, IO<sub>3</sub>= 0 V.

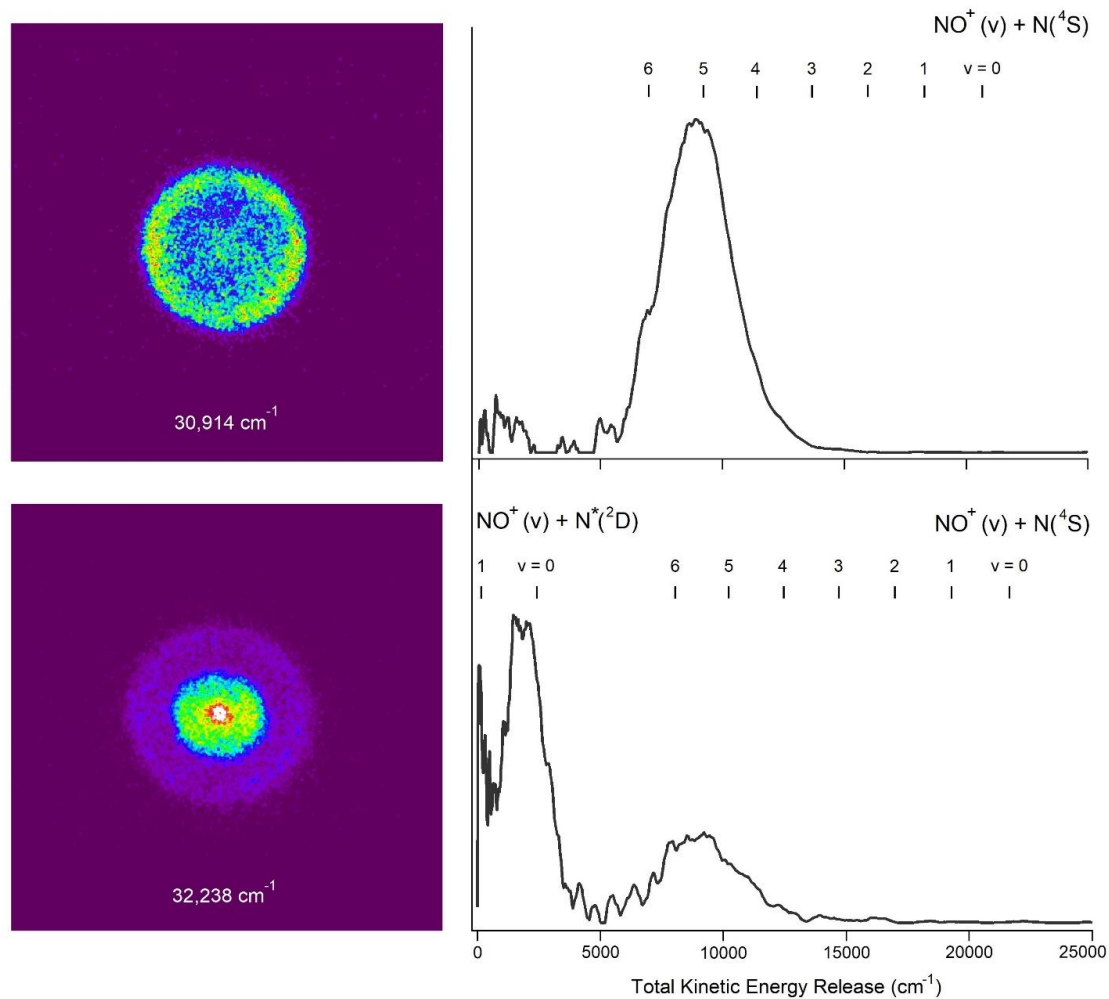


Figure 2.5. Raw photofragment images of  $\text{NO}^+$  made by dissociating  $\text{N}_2\text{O}^+$  at  $30,914 \text{ cm}^{-1}$  (top) and  $32,238 \text{ cm}^{-1}$  (bottom) and their corresponding velocity distributions converted to total kinetic energy release. Laser polarization is vertical in both cases.

## CHAPTER 3

### THE ALUMINUM DIMER CATION

#### 3.1 Introduction

The spectroscopy and dynamics of small metallic clusters has been an active area of research for several years.<sup>1-5</sup> Photofragment spectroscopy has been used to measure the bond dissociation energies ( $D_0$ ) of several transition metal-containing ions,<sup>6,7</sup> since these species often have at least one optically accessible excited electronic state near the dissociation threshold of the ground state.<sup>8</sup> In such cases, the observed thermodynamic onset of dissociation can provide accurate bond strengths.<sup>9</sup> However, the electronic structures of many other metal-containing species are not as accommodating, and the observed dissociation onset is spectroscopic rather than thermodynamic. If there are no excited states near  $D_0$ , the likelihood of finding a more useful electronic transition should be greater near the dissociative onset to form *electronically excited* products, since the overall density of states is higher there. Unfortunately, the photodissociation yield does not usually increase dramatically when the new product channel becomes accessible, making new thermodynamic onsets hard to identify.

Imaging the photofragments of ion beams<sup>10</sup> enables one to study the bond strengths and excited state dynamics of the many metal-containing species for which spectroscopy alone is insufficient. Photofragment imaging allows one to differentiate between detected fragment states through their unique kinetic energy releases (KER), making it possible to determine precise values of  $D_0$  at excitation energies near higher-lying product thresholds. In an imaging experiment, the KER is determined from the radial spread of ions at the detector, so the resolution of any  $D_0$  measurement is improved

when imaging fragments with lower KER. For this reason, it is often preferable to image metallic ions at energies near the first few electronically excited fragmentation onsets. Excitation energies in this region should be high enough to find a strong near-threshold transition, but low enough to avoid the more muddled transitions approaching the conduction band.

As the smallest aluminum cluster, the aluminum dimer represents the most fundamental system to study in an effort to identify chemical trends associated with increasing cluster size. Some collision induced dissociation (CID) experiments<sup>11, 12</sup> have measured the bond dissociation energy ( $D_0$ ) of  $Al_2^+$ . It has also been indirectly determined<sup>13</sup> by combining the ionization energies<sup>14</sup> of Al and  $Al_2$  with a re-evaluated Knudsen effusion measurement.<sup>15</sup> Table 3.1 compares these previously published experimental values alongside those obtained from selected theoretical works. Of note is the large discrepancy between the reported CID values. There is very little optical spectroscopy available in the published literature to benchmark the theoretical bond strengths and dissociation dynamics. So, it is a primary goal of this study to provide a more precise, direct measurement of the  $Al_2^+$  bond strength. Using high-level MRCI methods, Rosi *et al.*<sup>16</sup> characterized a few excited electronic states in  $Al_2^+$  with the potential for experimental confirmation given their high predicted oscillator strengths. The bound-to-unbound  $C\ ^2\Sigma_u^+ \leftarrow X\ ^2\Sigma_g^+$  transition is expected to give a broad, unstructured spectrum, which has been observed in very preliminary experiments.<sup>17</sup> Another excited state of particular interest, the so-called G  $^2\Sigma_u^+$  state, was predicted to have an unusual double-minimum potential energy surface that would greatly complicate its spectroscopy.

In this chapter, we use a combination of photodissociation spectroscopy, ion imaging, and high-level theory to elucidate the bond dissociation energy and photodissociation dynamics of the aluminum dimer cation from two excited states. The nature of the repulsive  $C^2\Sigma_u^+$  state is investigated and compared with previously published results. The predissociative  $G^2\Sigma_u^+$  state is also targeted for photodissociation because it is expected to lie very close to two excited state photoproduct thresholds, making it an excellent candidate for a bond dissociation energy measurement.

### 3.2 Methods

Photodissociation spectroscopy and imaging experiments were performed with the home-built fast ion photofragment imaging mass spectrometer described in the previous chapter. Aluminum dimer cations are formed by focusing the second harmonic output of a Nd:YAG laser (Continuum Minilite II) onto a rotating aluminum disc. A carrier gas mixture of 10% methane in helium is introduced by a pulsed solenoid valve (Parker series 9) into the laser ablation block, where it entrains the recently ablated aluminum ions before expanding into vacuum. The presence of methane in the gas mixture greatly enhances dimer production.

Theoretical potential energy surfaces for the ground and excited electronic states of  $Al_2^+$  below  $50,000\text{ cm}^{-1}$  were generated using multiple approaches. Calculations using a multireference configuration interaction (MRCI-F12) method with a large basis set (aug-cc-pVTZ) were performed with an MCSCF active space consisting of the 3s, 3p, 3d, and 4s orbitals on each aluminum atom. This is a larger active space than was used by Rosi *et al.* For comparison, an Equations-of-motion coupled cluster method with full

electron correlation and a large basis set (EOM-CCSD(Full)/aug-cc-pVQZ) was also used.

### 3.3 Theoretical Electronic Structure of $\text{Al}_2^+$

The MRCI calculated potentials of the electronic ground state and all relevant excited states below  $50,000 \text{ cm}^{-1}$  are shown in figure 3.1. Since one photon absorption from the  $X \ ^2\Sigma_g^+$  ground state to other gerade states is forbidden, only ungerade excited states are shown. For consistency, we have adopted the naming conventions and state labels that were originally used by Rosi *et al.* wherever possible.

The MRCI calculations presented here, along with those of Rosi *et al.*<sup>16</sup> predict an unbound  $C \ ^2\Sigma_u^+$  excited state with a large transition moment and a vertical excitation energy around  $24,800 \text{ cm}^{-1}$ . Saunders *et al.*<sup>18</sup> measured photodissociation of  $\text{Al}_x^+$  ( $x=2-8$ ) cluster ions at three photon energies. They observe modest dissociation at  $15,486 \text{ cm}^{-1}$ , less at  $19,438 \text{ cm}^{-1}$ , and none at  $28,068 \text{ cm}^{-1}$ . These results are inconsistent with the later simulated and measured absorption spectra of ground state  $\text{Al}_2^+$ , potentially due to dissociation of electronically excited  $\text{Al}_2^+$  ( $A \ ^2\Pi_u$ ) formed by the sputtering source.

The higher-lying  $G \ ^2\Sigma_u^+$  state is predicted to have two minima between  $35,000$  and  $40,000 \text{ cm}^{-1}$  with the relative depths of the wells being highly dependent on the level of theory used. This unusual shape is due to an avoided crossing with the  $G' \ ^2\Sigma_u^+$  state, which is expected to lie very near the vertical excitation from the ground state.

Transitions to the  $G \ ^2\Sigma_u^+$  state are predicted to be intense and the outer well (longer bond) consistently has a much higher electronic transition moment than the inner well. Rosi *et*

*al.* predicted that a great deal of complexity would arise in absorption spectra of the G  $^2\Sigma_u^+$  state as a result of this highly anharmonic behavior.

Our calculations suggest that the G  $^2\Sigma_u^+$  state dissociates adiabatically to Al ( $^2S$ ) fragments after overcoming a barrier at 5.4 Å, while the prior work predicts that the G  $^2\Sigma_u^+$  state correlates to higher energy products. This highlights a key difference between the calculations presented here and the earlier results of Rosi. The earlier study doesn't include the  $^2\Pi_u$  state seen here just below G  $^2\Sigma_u^+$  or any excited potential energy surfaces that correlate to the Al ( $^2S$ ) channel. These discrepancies are almost certainly due to the smaller (3s, 3p) active space employed. Today, of course, the computational burden of running a larger (3s, 3p, 3d, 4s) MCSCF active space is not as prohibitive as it was in 1991.

### 3.4 Photodissociation Spectra of Al<sub>2</sub><sup>+</sup>

The photodissociation spectra of Al<sub>2</sub><sup>+</sup> from 20,000 – 23,800 cm<sup>-1</sup> and 38,500 – 42,000 cm<sup>-1</sup> were recorded by monitoring the production of Al<sup>+</sup> fragments while slowly scanning the photolysis laser energy (step size = 0.02 nm). The final spectra are the average of several scans, which have been corrected for fluctuations in laser power and changes in parent (Al<sub>2</sub><sup>+</sup>) intensity over time.

As expected, Al<sub>2</sub><sup>+</sup> absorbs broadly from 20,000 – 23,800 cm<sup>-1</sup> due to the C  $^2\Sigma_u^+ \leftarrow$  X  $^2\Sigma_g^+$  transition. The peak of fragmentation signal in this region is near 23,250 cm<sup>-1</sup>. The 38,500 – 42,000 cm<sup>-1</sup> spectrum (Figure 3.2), which results from the G  $^2\Sigma_u^+ \leftarrow$  X  $^2\Sigma_g^+$  transition, is structured and quite complicated. As the transition energy is increased,

broad peaks of low intensity eventually give way to much sharper and higher intensity features.

The  $G\ ^2\Sigma_u^+$  state is predicted to be the dominant optically accessible electronic state in this energy region; it is a fully allowed transition from the ground state ( $X\ ^2\Sigma_g^+$ ). Only minor contributions from other nearby excited states ( $^2\Pi_u$  and  $G'\ ^2\Sigma_u^+$ ) are expected. As predicted, the spacings and amplitudes in the observed vibronic progression are quite anharmonic, making the spectrum difficult to characterize precisely. However, scans at various temperatures and the corresponding simulated spectra have helped us identify several transitions that originate from  $v'' = 0$  and  $v'' = 1$  in  $X\ ^2\Sigma_g^+$ , thus allowing us to measure the ground state vibrational fundamental  $\nu_0 = 172\text{ cm}^{-1}$ . Our value compares favorably with the resonant two photon ionization measurement of Harrington and Weisshaar<sup>14</sup> ( $\omega_e = 178 \pm 8\text{ cm}^{-1}$ ) and the harmonic frequencies calculated by Kiohara *et al.*<sup>19</sup> ( $\omega_e = 171\text{ cm}^{-1}$ ), Rosi *et al.*<sup>16</sup> ( $\omega_e = 173\text{ cm}^{-1}$ ), and Bauschlicher *et al.*<sup>20</sup> ( $\omega_e = 169\text{ cm}^{-1}$ ). The average spacing between vibronic transitions to  $G\ ^2\Sigma_u^+$  originating from  $X\ ^2\Sigma_g^+$  ( $v'' = 0$ ) is  $\sim 170\text{ cm}^{-1}$ , which is in good agreement with Rosi's harmonic frequency for the outer well of  $G\ ^2\Sigma_u^+$  ( $\omega_e = 177\text{ cm}^{-1}$ ), especially considering how dependent the nature of the  $G\ ^2\Sigma_u^+$  state is on level of theory used.

Using the  $G\ ^2\Sigma_u^+ \leftarrow X\ ^2\Sigma_g^+$  band, we estimate the integrated oscillator strength as  $f = 0.0039$ . This is surprisingly low for a fully allowed bound-to-bound transition, which suggests the existence of an alternate energy disposal process, specifically fluorescence. The likelihood of a competing fluorescence process is supported by the short fluorescence lifetimes calculated by Rosi *et al.*<sup>16</sup> The authors report lifetimes on the order of 1 ns for  $G\ ^2\Sigma_u^+$  ( $v = 10-14$ ), vibrational wavefunctions which are predicted to sample

the high oscillator strength of the outer well. A potential competition between emission and dissociation pathways is another complicating factor in the photodissociation spectrum of  $G\ ^2\Sigma_u^+ \leftarrow X\ ^2\Sigma_g^+$  as the relative probability of either event occurring would be highly dependent on the specific vibrational state being populated in  $G\ ^2\Sigma_u^+$ . This suggests that laser-induced fluorescence studies of the  $G\ ^2\Sigma_u^+ \leftarrow X\ ^2\Sigma_g^+$  band could be performed to further characterize  $Al_2^+$ .

### 3.5 Images of $Al^+$ Fragments

Photofragment images were recorded by tuning the photolysis laser to the energy of a specific transition in the photodissociation spectrum and monitoring the  $Al^+$  product. Under the conditions of this study, the photodissociation of  $Al_2^+$  yields one ionized and one neutral atomic aluminum fragment. It is usually preferable to detect the lighter product of a dissociation event due to the improved resolution that it affords. However, a common challenge encountered when imaging metal-containing systems is that the heavier metallic fragment very often carries away the charge. Being a dimer cation,  $Al_2^+$  has the benefit of comparatively good kinematics. The detected ion ( $Al^+$ ) departs with the same transverse velocity as the cofragment ( $Al$ ), reducing the relative kinetic energy per pixel, thereby improving the resolution. The photon energy is not sufficient to produce electronically excited  $Al^+$ , so the detected fragment is always in its ground state ( $^1S$ ). For brevity, the following text will discuss the possible photofragment channels only in terms of the state of the neutral cofragment.

### 3.5.1 Images from ( $C\ ^2\Sigma_u^+ \leftarrow X\ ^2\Sigma_g^+$ )

The behavior of the  $C\ ^2\Sigma_u^+$  state is further confirmed by imaging, which reveals a single highly anisotropic ( $\beta=2$ ) product channel (Figure 3.3) across the entirety of the broad photodissociation spectrum (20,000 – 23,800  $\text{cm}^{-1}$ ). The majority of the fragment intensity in the images is located at the poles, indicating prompt dissociation via the predicted parallel transition ( $C\ ^2\Sigma_u^+ \leftarrow X\ ^2\Sigma_g^+$ ). A transition to this unbound state yields fragments in their ground electronic states that have a fair amount of KER. The undetected cofragment, Al ( $^2P^\circ$ ), has two spin-orbit states split by 112  $\text{cm}^{-1}$  that are not resolved. Images of photolyzed  $Al_2^+$  recorded at several wavelengths in this spectral region give an average  $D_0$  of  $138 \pm 5$  kJ/mol, which compares favorably with the previous benchmark.<sup>13</sup>

It is worth noting that, at the peak of absorption for the  $C\ ^2\Sigma_u^+ \leftarrow X\ ^2\Sigma_g^+$  transition in  $Al_2^+$ , the total KER is nearly 12,000  $\text{cm}^{-1}$  above the only accessible dissociation threshold. Since the only remaining destination for that excess energy is in the form of KER, the ring radii of images taken in this region are quite large. The measured KER is proportional to the radius squared, so its error increases proportionally with the radius. This highlights an inherent source of error in our, and indeed all, ion imaging experiments in which the photolysis energy is significantly greater than the dissociation limit of interest. For this reason,  $Al_2^+$  was next imaged in the UV, where theory predicts intense transitions to the  $G\ ^2\Sigma_u^+$  state lie at energies that are much closer to those of excited state product thresholds.

### 3.5.2 Images from ( $G^2\Sigma_u^+ \leftarrow X^2\Sigma_g^+$ )

Images recorded below  $40,400\text{ cm}^{-1}$ , like the one shown in figure 3.4, indicate that  $\text{Al}_2^+$  primarily dissociates to form ground state Al ( $^2P^\circ$ ) with a significant amount of KER. These high velocity fragments likely form by coupling to, and rebounding off the repulsive wall of  $C^2\Sigma_u^+$ . A minor channel at lower KER corresponds to production of Al ( $^2S$ ),  $25,348\text{ cm}^{-1}$  above the  $^2P_{1/2}^\circ$  ground state. Two possible mechanisms for this are: tunneling through the barrier in the  $G^2\Sigma_u^+$  state at  $\sim 5\text{ \AA}$ , or bypassing the barrier via intersystem crossing to, and then back from, the  $c^4\Pi_u$  state on either side of it. Although the features in this region of the photodissociation spectrum are reproducible, they are small, cluttered, and very difficult to characterize. Thus, imaging below  $40,400\text{ cm}^{-1}$  is not ideal for the determination of a precise bond dissociation energy.

Above  $40,400\text{ cm}^{-1}$ , where the transitions are more intense and relatively clean, images reveal the production of spin-forbidden Al ( $^4P$ ) fragments. The photofragment image shown in figure 3.5 is typical of images recorded above the energetic threshold for Al ( $^4P$ ) products ( $40,479\text{ cm}^{-1}$ ). One can determine the relative product branching ratios by calculating the integrated signal under each ring in an image. We find that Al ( $^4P$ ) fragments account for no less than 90% of the total intensity in any image recorded above the corresponding threshold. It is surprising that photodissociation favors spin-forbidden products over the lower energy, spin-allowed pathways. We believe that the quartet channel dominates because the populated vibrational wavefunctions of  $G^2\Sigma_u^+$  actually have stronger coupling to the nearby barrier-less quartet potential ( $c^4\Pi_u$ ) via the spin-orbit interaction than they do through relatively poor Frank-Condon overlap with directly dissociative doublet states like  $C^2\Sigma_u^+$ ,  $A^2\Sigma_u^+$ , or the repulsive side of the  $G^2\Sigma_u^+$  potential

( $r > 5.4 \text{ \AA}$ ). Based on the calculated potential energy surfaces, it is expected that the Al ( $^2\text{S}$ ) pathway will eventually dominate the Al ( $^4\text{P}$ ) channel when the excitation energy is sufficient to overcome the aforementioned G  $^2\Sigma^+_u$  barrier ( $43,000 \text{ cm}^{-1}$ ). Unfortunately, the excitation energy required to surmount the barrier is above the range of this experiment. The photofragment images of all product channels observed in the present photodissociation range are isotropic, indicating that the dissociative lifetimes from the G  $^2\Sigma^+_u$  state are consistently longer than the rotational period of  $\text{Al}_2^+$ .

It is worth comparing the electronic structures and spectroscopies of  $\text{Al}_2^+$  with those of neutral  $\text{Al}_2$  because the neutral has several states that behave similarly to those probed by the current study. The potential energy surfaces that describe the 1, 2, and 3  $^3\Pi_g$  states of the neutral exhibit behavior that closely resembles that of the C1  $^2\Sigma^+_u$ , G2  $^2\Sigma^+_u$ , and G'3  $^2\Sigma^+_u$  states of the cation. In each case, state 1 is repulsive and is thought to predissociate states 2 and 3. An avoided crossing between states 2 and 3 results in state 2 being skewed in the neutral and having two minima in the cation. State 3 also has an anomalously high vibrational frequency in both cases. For both molecules, transitions from the ground state to all three excited states (particularly state 2) are intense.<sup>21</sup> However, there are interesting differences between the excited states of these two species in their relative rates of radiative and non-radiative decay. For state 2 in  $\text{Al}_2$ , quick (1-100 ps) radiationless decay into ground state Al fragments is predicted to dominate the relatively lengthy ( $>100 \text{ ns}$ ) emission process.<sup>13, 21, 22</sup> The short lifetime for this state is consistent with its detection by absorption<sup>23</sup> and not via REMPI.<sup>13</sup> For  $\text{Al}_2^+$  on the other hand, the shorter calculated fluorescence lifetimes ( $\sim 1 \text{ ns}$ ) and the photodissociation data mentioned in section 3.4 point to a much more competitive radiative decay pathway.

Another major benefit of imaging the fragments of  $\text{Al}_2^+$  in this near-threshold region is the minimal amount of extrapolation necessary to determine  $D_0$ . A series of images recorded in this region were analyzed for total KER and plotted as a function of excitation energy. The resulting trend is shown in figure 3.6 and is the result of imaging on transitions that are assigned to  $v'' = 0$ , so that the internal energy of the parent is well known. The bond dissociation energy is determined by subtracting the total internal energy of the relevant fragments<sup>24</sup> from the y-intercept of the trendline. Using this method, the bond dissociation energy of  $\text{Al}_2^+$  ( $X^2\Sigma_g^+$ ) is found to be  $136.6 \pm 1.8$  kJ/mol. The main contributor to the final uncertainty in  $D_0$  is our inability to resolve the three spin-orbit states of Al ( $^4P$ ), which all lie within a range of  $120 \text{ cm}^{-1}$ . As shown in table 3.1, our value is consistent with, but substantially more precise than the CID measurement of Ingolfsson *et al.*<sup>12</sup>. It also confirms and improves upon the indirect measurement of Fu *et al.*<sup>13</sup> The  $D_0$  values obtained from *ab initio* calculations are in excellent agreement with our VMI measurement, while DFT methods tend to overestimate it.<sup>19</sup> In addition, the bond dissociation energy of  $\text{Al}_2^+$  can be used to determine the bond strength of neutral aluminum dimer using the following equation:

$$D_0(\text{Al}_2) + IE(\text{Al}) = D_0(\text{Al}_2^+) + IE(\text{Al}_2) \quad (3.1)$$

Using the ionization energies (IE) determined by Harrington and Weisshaar,<sup>14</sup> the bond dissociation energy of the neutral is  $D_0(\text{Al}_2) = 129 \pm 6$  kJ/mol. This refines the neutral bond strength determined by Fu *et al.*<sup>13</sup> through reanalysis of the original Knudsen effusion data of Stearns and Kohl.<sup>15</sup>

### 3.6 Conclusions

The photodissociation dynamics of  $\text{Al}_2^+$  have been investigated by photodissociation spectroscopy and photofragment imaging in the 20,000 – 23,800  $\text{cm}^{-1}$  and 38,500 – 42,000  $\text{cm}^{-1}$  ranges. These experiments are compared to theory at the EOM-CCSD(full)/aug-cc-pVQZ and MRCI-F12/aug-cc-pVTZ levels in order to further elucidate the complex nature of the aluminum dimer cation excited states. As expected, the directly dissociative  $\text{C } ^2\Sigma_u^+ \leftarrow \text{X } ^2\Sigma_g^+$  transition yields ground state photoproducts with extreme parallel anisotropy and a large amount of KER. Calculations predict that the  $\text{G } ^2\Sigma_u^+$  potential energy surface has two minima due to an avoided crossing very close to the geometry of the ground state. This behavior is manifested in the extremely anharmonic photodissociation spectrum of the corresponding region. Analysis of photodissociation spectra at various temperatures gives  $\nu_0 = 172 \text{ cm}^{-1}$  for the ground state ( $\text{X } ^2\Sigma_g^+$ ) and an average vibrational spacing of  $170 \text{ cm}^{-1}$  for the excited state ( $\text{G } ^2\Sigma_u^+$ ). The relatively low photofragment yield from  $\text{G } ^2\Sigma_u^+ \leftarrow \text{X } ^2\Sigma_g^+$  is explained by a likely competition between relatively fast fluorescence and several different non-radiative dissociation pathways. Photofragment images reveal that, once energetically accessible, spin-forbidden  $\text{Al } (^4\text{P})$  products immediately dominate the lower energy  $\text{Al } (^2\text{P}^\circ)$  and  $\text{Al } (^2\text{S})$  channels. It is predicted that the  $\text{G } ^2\Sigma_u^+$  state eventually correlates adiabatically to  $\text{Al } (^2\text{S})$  products after a wide barrier at larger bond lengths. Thus, it is expected that the spin-allowed  $\text{Al } (^2\text{S})$  channel will be favored over the  $\text{Al } (^4\text{P})$  pathway once the excitation energy surpasses the barrier height. Analysis of the radial distribution of  $\text{Al}^+$  fragments gives an improved experimental measurement of the bond strength of  $\text{Al}_2^+$  ( $D_0 = 136.6 \pm$

1.8 kJ/mol). Combining this result with the ionization energies of Al and Al<sub>2</sub> also refines the bond strength of the neutral dimer ( $D_0 = 136.9 \pm 1.8$  kJ/mol).

### 3.7 References

1. W. A. Deheer, Rev. Mod. Phys. **65**, 611-676 (1993).
2. M. Brack, Rev. Mod. Phys. **65**, 677-732 (1993).
3. E. C. Tyo and S. Vajda, Nat. Nanotechnol. **10**, 577-588 (2015).
4. *Gas-Phase Cluster Ions*, edited by M. T. Bowers, M. F. Jarrold and A. J. Stock, Special Issue. Int. J. Mass. Spectrom. Ion. Proc., (Elsevier, Amsterdam, 1990).
5. P. B. Armentrout, Annu. Rev. Phys. Chem. **52**, 423-461 (2001).
6. D. J. Matthew, E. Tieu and M. D. Morse, J. Chem. Phys. **146**, 10 (2017).
7. A. Sevy, J. J. Sorensen, T. D. Persinger, J. A. Franchina, E. L. Johnson and M. D. Morse, J. Chem. Phys. **147**, 8 (2017).
8. C. J. Cassady and B. S. Freiser, J. Am. Chem. Soc. **106**, 6176-6179 (1984).
9. D. R. A. Ranatunga and B. S. Freiser, Chem. Phys. Lett. **233**, 319-323 (1994).
10. D. W. Chandler and P. L. Houston, J. Chem. Phys. **87**, 1445-1447 (1987).
11. L. Hanley, S. A. Ruatta and S. L. Anderson, J. Chem. Phys. **87**, 260-268 (1987).
12. O. Ingólfsson, H. Takeo and S. Nonose, J. Chem. Phys. **110**, 4382-4393 (1999).
13. Z. W. Fu, G. W. Lemire, G. A. Bishea and M. D. Morse, J. Chem. Phys. **93**, 8420-8441 (1990).
14. J. E. Harrington and J. C. Weisshaar, J. Chem. Phys. **93**, 854-855 (1990).
15. C. A. Stearns and F. J. Kohl, High Temp. Sci. **5**, 113-127 (1973).
16. M. Rosi, C. W. Bauschlicher Jr. and S. R. Langhoff, Chem. Phys. **151**, 1-9 (1991).
17. *Personal communication in reference 16.*
18. W. A. Saunders, P. Fayet and L. Woste, Phys. Rev. A **39**, 4400-4405 (1989).
19. V. O. Kiohara, E. F. V. Carvalho, C. W. A. Paschoal, F. B. C. Machado and O. Roberto-Neto, Chem. Phys. Lett. **568**, 42-48 (2013).

20. C. W. Bauschlicher Jr., L. A. Barnes and P. R. Taylor, *J. Phys. Chem.* **93**, 2932-2935 (1989).
21. S. Han, H. Hetteima and D. R. Yarkony, *J. Chem. Phys.* **102**, 1955-1964 (1995).
22. M. F. Cai, C. C. Carter, T. A. Miller and V. E. Bondybey, *Chem. Phys.* **155**, 233-245 (1991).
23. J. J. Scherer, J. B. Paul and R. J. Saykally, *Chem. Phys. Lett.* **242**, 395-400 (1995).
24. A. Kramida, Y. Ralchenko, J. Reader and NIST ASD Team. (2018). *NIST Atomic Spectra Database (Version 5.5.2)*, Available: <http://physics.nist.gov/asd>. (National Institute of Standards and Technology, Gaithersburg, MD)
25. K. K. Sunil and K. D. Jordan, *J. Phys. Chem.* **92**, 2774-2781 (1988).

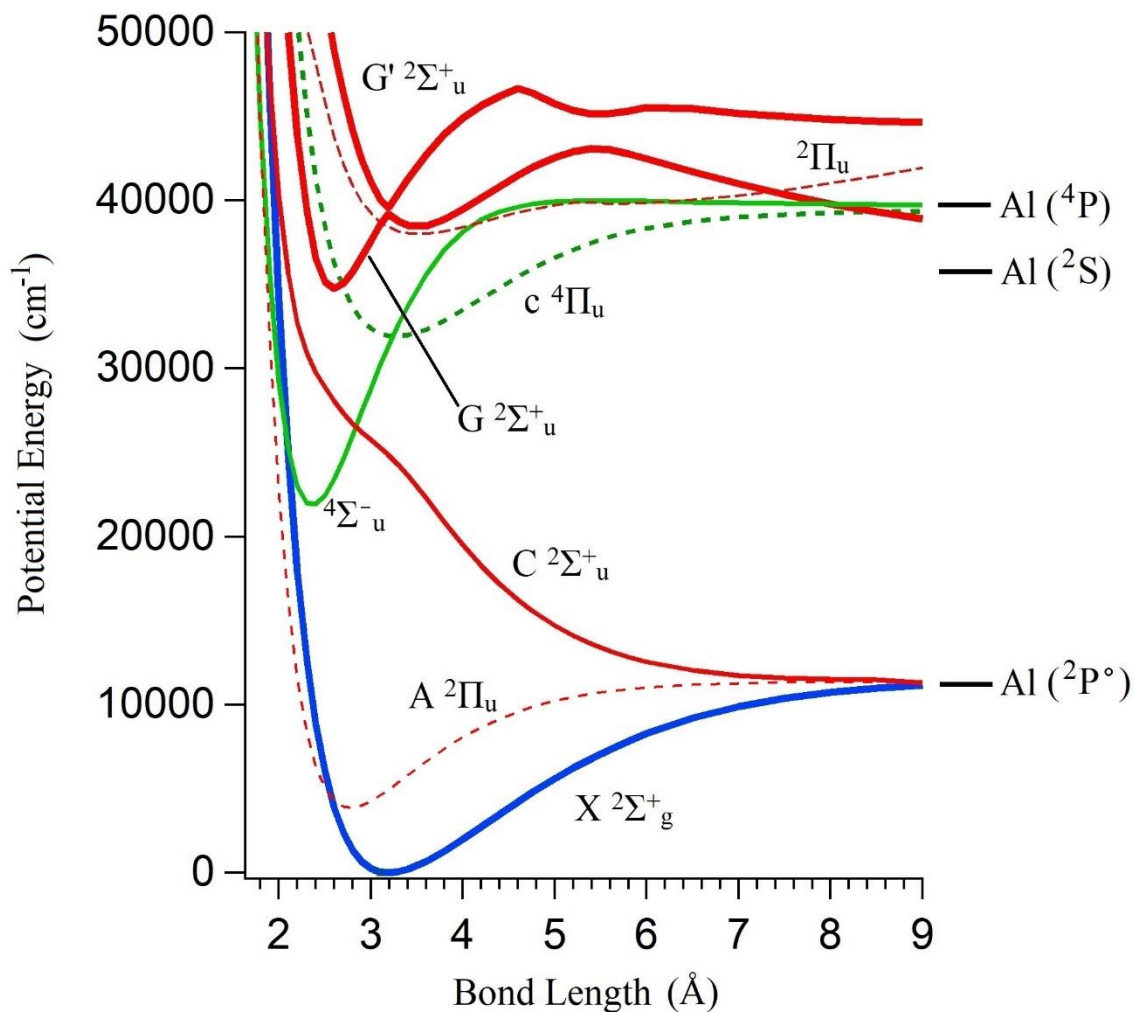


Figure 3.1. Relevant MRCI-F12/aug-cc-pVTZ calculated potential energy surfaces for excited states of  $\text{Al}_2^+$  below  $50,000 \text{ cm}^{-1}$ . The ground state ( $X \ ^2\Sigma^+_g$ ) is shown in blue. The optically accessible ungerade doublet states are in red. Dashed lines represent  $\Pi$  states and green lines represent quartet states. Aluminum photofragment thresholds are indicated on the right; the fragment channels are labeled according to the resulting atomic state of the neutral Al cofragment since  $\text{Al}^+$  remains in the ground state at all energies reached in this study.

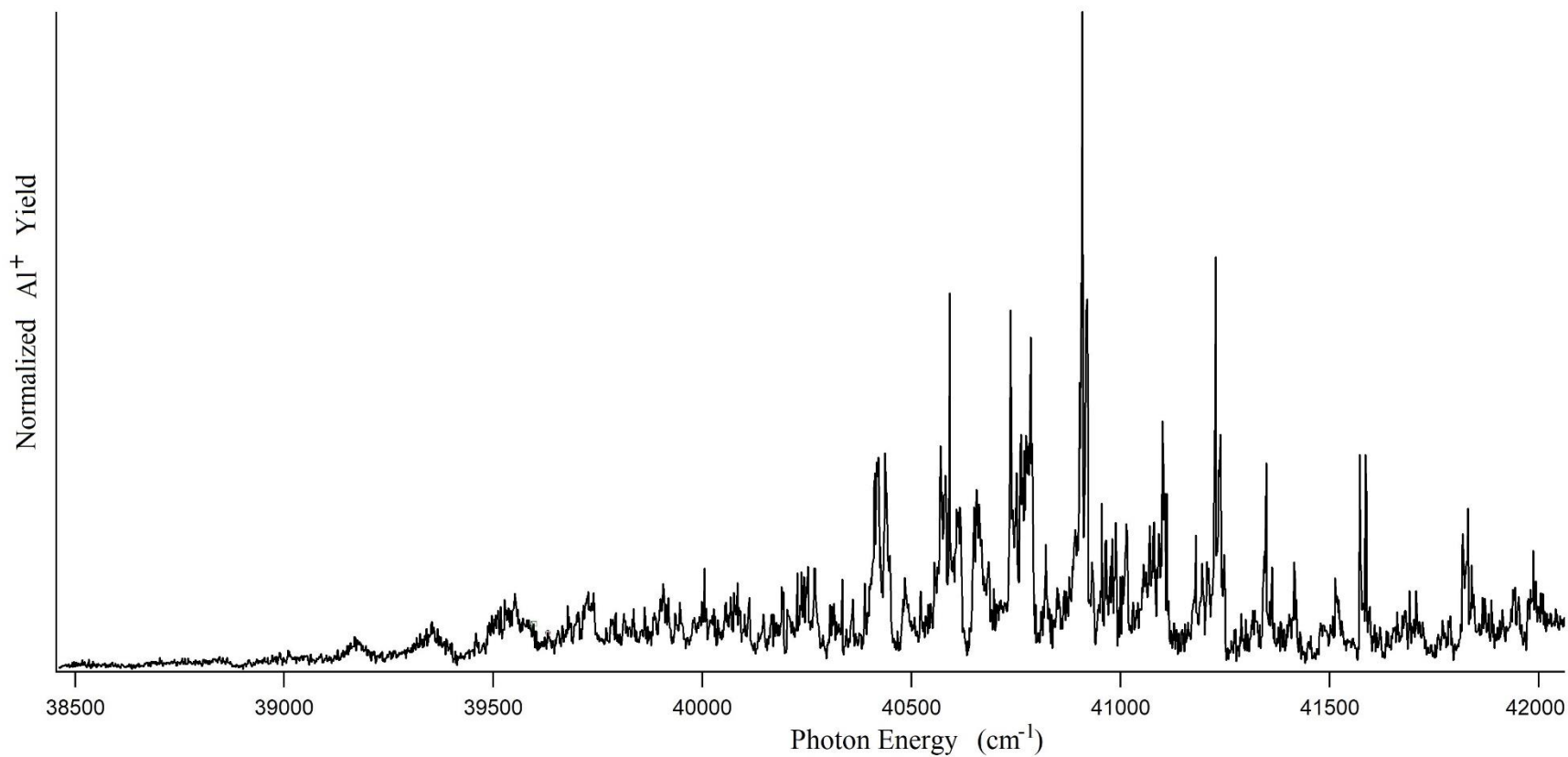


Figure 3.2. Photodissociation spectrum of  $\text{Al}_2^+$  in the  $\text{G } ^2\Sigma_u^+ \leftarrow \text{X } ^2\Sigma_g^+$  transition region.

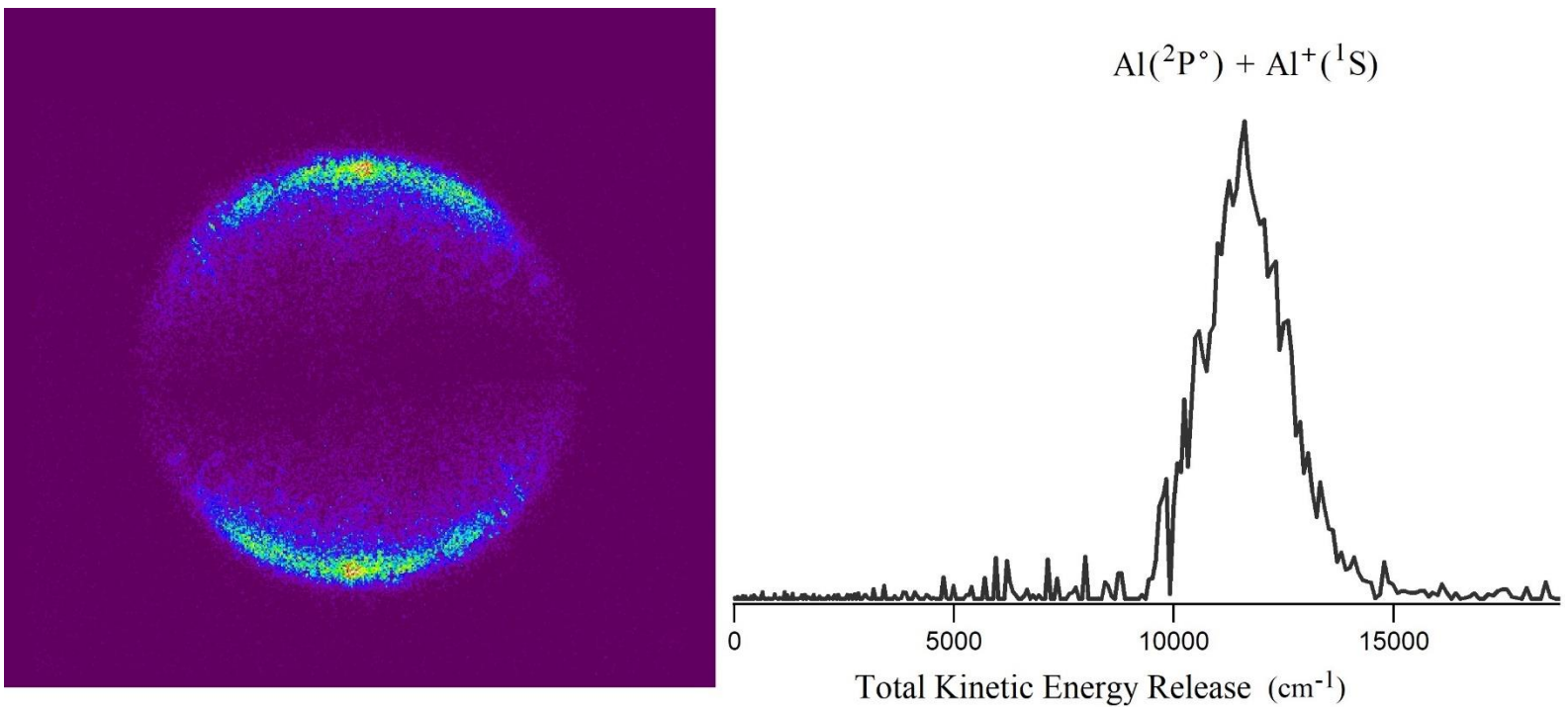


Figure 3.3. Photofragment image of  $\text{Al}^+$  made by dissociating  $\text{Al}_2^+$  at  $23,669 \text{ cm}^{-1}$  and the corresponding velocity distribution converted to total kinetic energy release. The image shown has been top/bottom symmetrized with a center of inversion. Laser polarization is vertical.

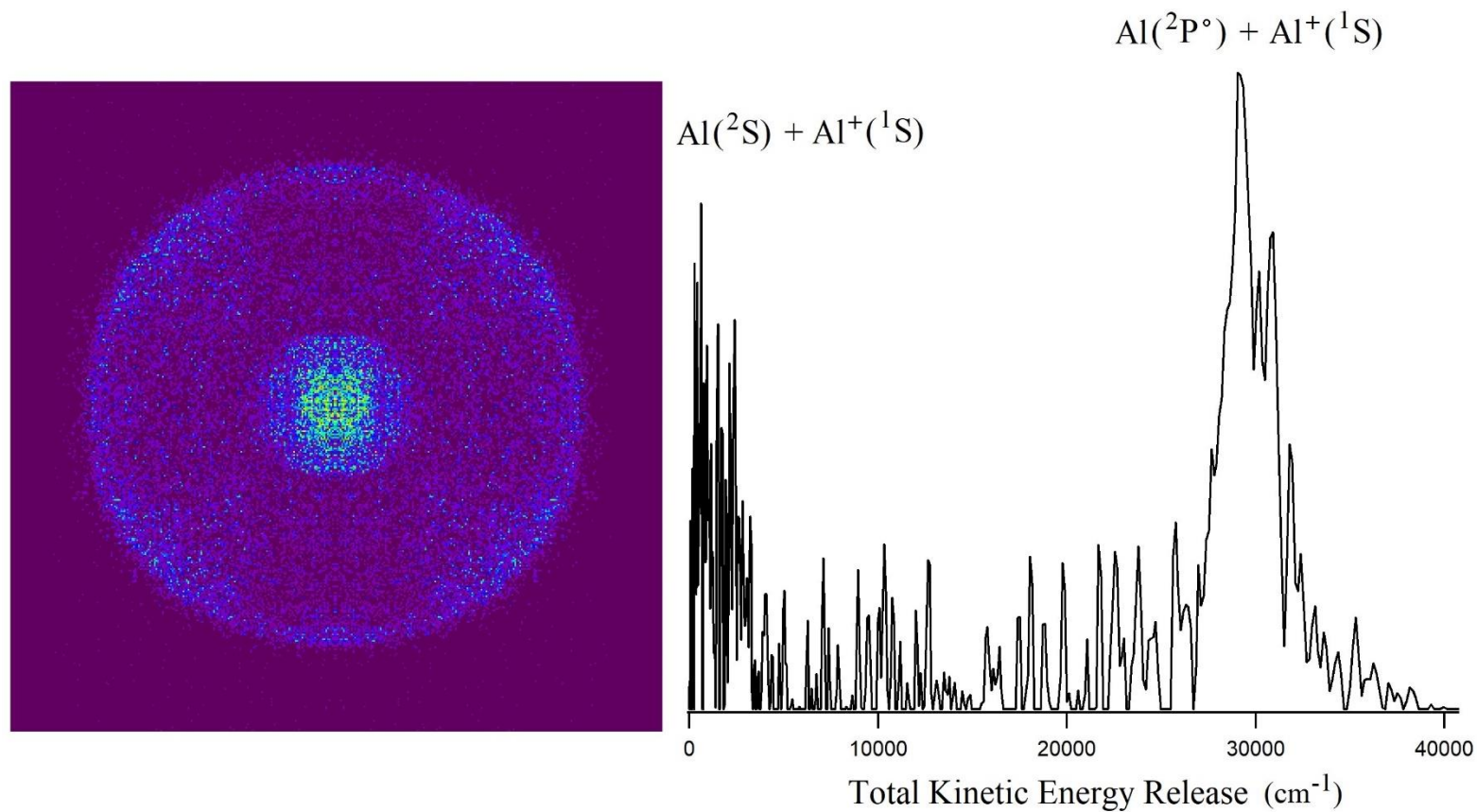


Figure 3.4. Photofragment image of  $\text{Al}^+$  made by dissociating  $\text{Al}_2^+$  at  $39,703 \text{ cm}^{-1}$  and the corresponding velocity distribution converted to total kinetic energy release. The image shown has been top/bottom and left/right symmetrized. Laser polarization is vertical.

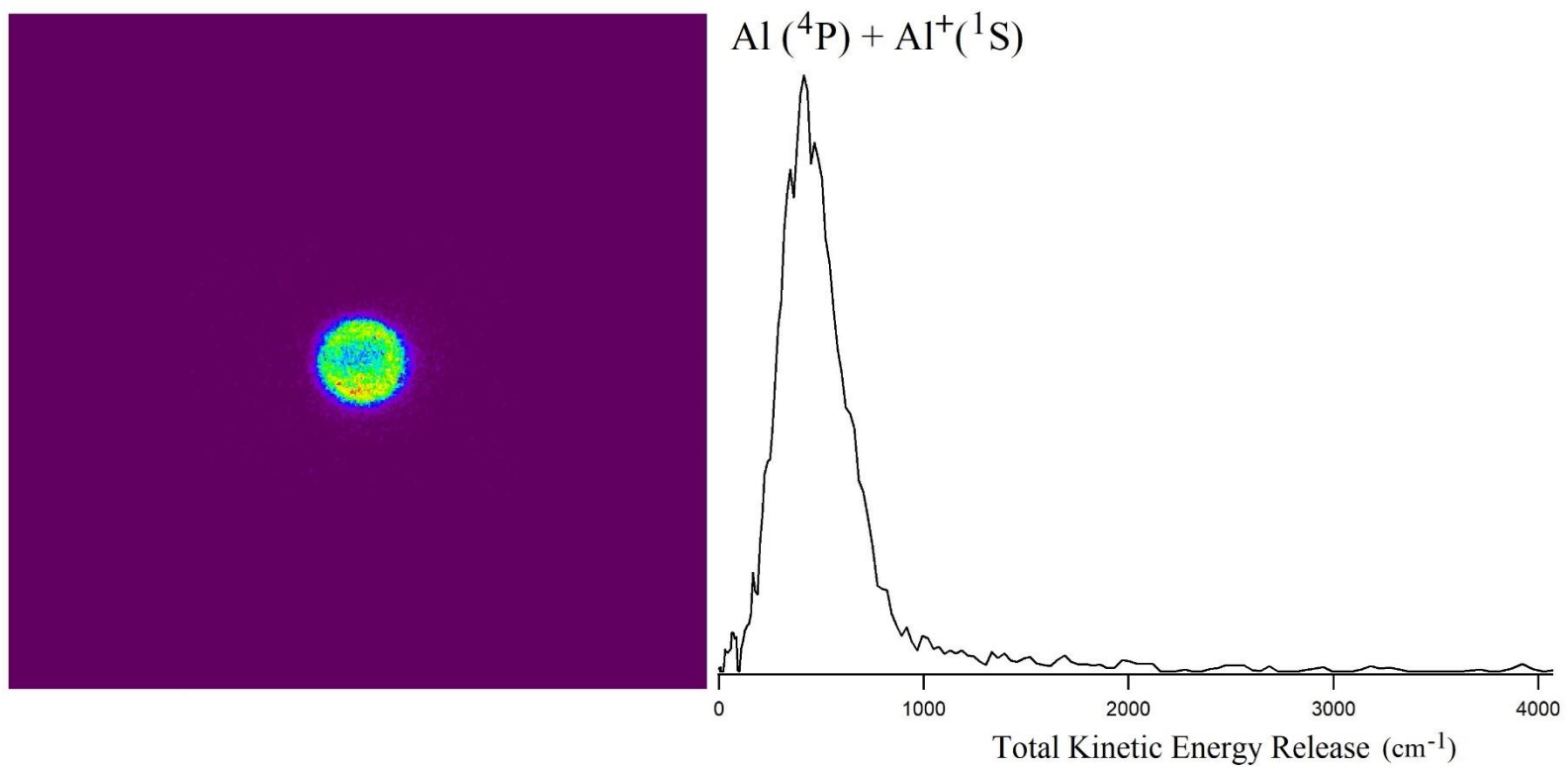


Figure 3.5. Photofragment image of Al<sup>+</sup> made by dissociating Al<sub>2</sub><sup>+</sup> at 40,922 cm<sup>-1</sup> and the corresponding velocity distribution converted to total kinetic energy release. Laser polarization is vertical.

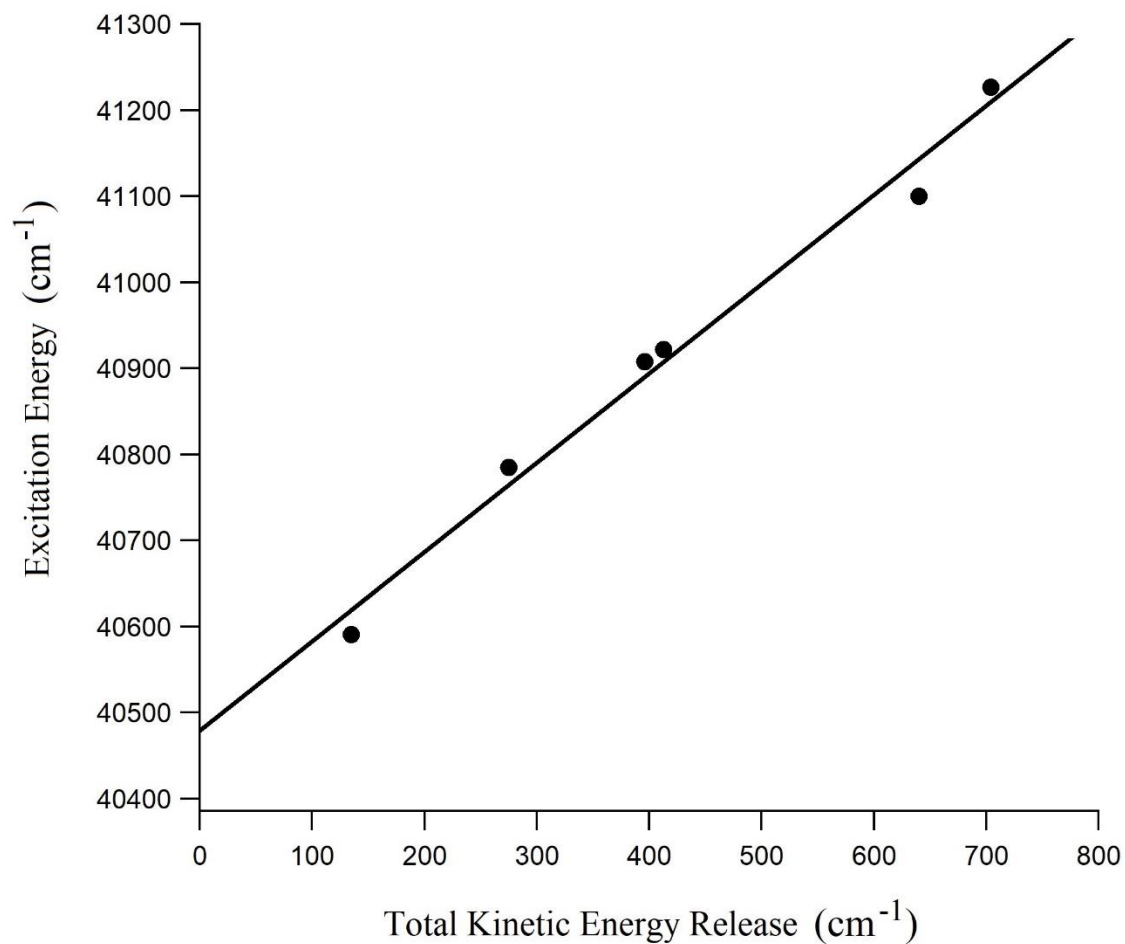


Figure 3.6. Plot of excitation energy versus total kinetic energy release for several images of  $\text{Al}^+$  products resulting from photodissociation of cold  $\text{Al}_2^+$ . The bond dissociation energy ( $D_0$ ) of  $\text{Al}_2^+$  is obtained by subtracting the known  $\text{Al}(^4\text{P})$  excitation energy from the y-intercept of the linear fit.

Table 3.1. Experimental and theoretical bond dissociation energies ( $D_0$ ) of  $\text{Al}_2^+$  ( $^2\Sigma_g^+$ ).

$D_0$ of $\text{Al}_2^+$ (kJ/mol)	Experiment
$87 \pm 29$	CID <sup>11</sup>
$121 \pm 35$	CID <sup>12</sup>
$129 \pm 6$	Neutral $D_0$ and IE with atomic IE <sup>13</sup>
$138 \pm 5$	VMI ( $C^2\Sigma_u^+ \leftarrow X^2\Sigma_g^+$ )(present study)
$136.6 \pm 1.8$	VMI ( $G^2\Sigma_u^+ \leftarrow X^2\Sigma_g^+$ )(present study)
	<b>Theory<sup>a</sup></b>
131	CCD + ST(CCD) <sup>25</sup>
136	MRCI <sup>20</sup>
137	CCSD(T)/aug-cc-pVQZ <sup>19</sup>
154	PBE0/aug-cc-pVTZ <sup>19</sup>
156	M05/aug-cc-pVTZ <sup>19</sup>
154	M06/aug-cc-pVTZ <sup>19</sup>

<sup>a</sup>  $D_e$  values obtained from theory were converted to  $D_0$  by subtracting a zero-point energy of 1 kJ/mol

## CHAPTER 4

### THE MANGANESE OXIDE CATION

#### 4.1 Introduction

Transition metal oxide cations and their roles in catalytic activation have been the subject of much experimental and theoretical research for several decades.<sup>1,2</sup>  $\text{MnO}^+$  is known to activate C-H bonds efficiently,<sup>3</sup> and the formation of methanol from its reaction with methane is exothermic. Yet, unlike some other transition metal oxides, it mostly reacts via hydrogen abstraction and its reaction with methane primarily yields  $\text{MnOH}^+$  instead of the more desirable methanol product.<sup>3-5</sup> Uncertainty remains regarding the precise electronic structure and properties of  $\text{MnO}^+$ , which have proven to be quite challenging to model theoretically.<sup>6</sup> The computational difficulties associated with  $\text{MnO}^+$  arise from the highly multi-reference nature of the ground state and numerous low-lying excited states. Density functional theory (DFT) approaches in particular are known to produce highly variable results depending on the method and basis set used. Although all recent high-level calculations agree that the ground state is  $^5\Pi$ , several older calculations, even at levels as sophisticated as CASPT2D (complete active space, with second order perturbation theory) predict that the ground state is  $^5\Sigma^+$ .<sup>3</sup> Despite the computational burden imposed by the presence of high-spin manganese, very high level electronic structure calculations of  $\text{MnO}^+$  have been done by Miliordos *et al.*<sup>7</sup> However, these studies, while thorough, are limited in scope, and only consider a handful of excited quintet states. On top of this, experimental studies of  $\text{MnO}^+$  are sparse and the spectroscopy is virtually unknown. The bond dissociation energy was measured by

Armentrout *et al.*<sup>8</sup> using an ion beam technique ( $D_0 = 239 \pm 10$  kJ/mol); a subsequent ion beam measurement gave a substantially higher value ( $D_0 = 285 \pm 13$  kJ/mol).<sup>9</sup>

Photofragment imaging has proven an effective way to determine bond dissociation energies from less spectroscopically useful repulsive states. However, imaging measurements tend to be more precise when taken closer to a corresponding product threshold. Fortunately, it is expected that  $\text{MnO}^+$ , like other transition metal species, has a greater density of states near the higher energy thresholds of excited dissociation products. In this study, we use theory at the TD-DFT, EOM-CCSD, and MRCI level along with photodissociation spectroscopy and ion imaging in order to explore the electronic structure and dynamics of  $\text{MnO}^+$ . In section 4.3, we report the photodissociation spectrum from 21,300 – 33,900  $\text{cm}^{-1}$ ; it is quite structured and contains transitions to several excited electronic states. Then, in section 4.4, photofragment images recorded at multiple wavelengths near the first excited  $\text{Mn}^{+*} (^5\text{S}) + \text{O} (^3\text{P})$  threshold are discussed. The kinetic energy release (KER) measured from these images allows us to determine the bond strength of  $\text{MnO}^+$ .

## 4.2 Methods

The experimental scheme used in the present study is described in detail in Chapter 2. Manganese oxide cations are created by ablating a rotating manganese disc with the second harmonic output of a Nd:YAG laser (Continuum Minilite II) in the presence of a pulsed gas mixture (10%  $\text{N}_2\text{O}$  in He). A buffer gas of pure helium was used in the trap, as  $\text{MnO}^+$  is known to react rapidly with hydrogen.<sup>3</sup> The proclivity of  $\text{MnO}^+$  to

react with hydrogen and produce heavier species was, at times, used to help distinguish it from the nearby  $\text{MnOH}^+$  and  $\text{MnOH}_2^+$  peaks in the mass spectrum.

The ground and several excited electronic states of  $\text{MnO}^+$  were calculated using a variety of electronic structure methods. *Gaussian09*<sup>10</sup> was used for ground state calculations at the density functional (B3LYP) and coupled cluster (CCSD and CCSD(T)) level, as well as for excited state calculations using time-dependent density functional theory (TD-DFT) and equations-of-motion CCSD (EOM-CCSD). *Molpro*<sup>11, 12</sup> software was used for multi-reference configuration interaction (MRCI) calculations analogous to those of Miliordos *et al.*,<sup>7</sup> but seeking to characterize higher-lying states.

#### 4.3 Theoretical Electronic Structure of $\text{MnO}^+$

The density functional and coupled cluster calculations predict that  $\text{MnO}^+$  has a  $^5\Pi$  ground state, in accord with recent high-level calculations. At the B3LYP/6-311++G(3df,3pd) level, the ground state has  $r_e = 1.729 \text{ \AA}$  and a harmonic vibrational frequency of  $\omega_e = 642 \text{ cm}^{-1}$ . The  $^5\Sigma^+$  excited state is calculated to be only  $1832 \text{ cm}^{-1}$  higher in energy ( $T_e$ ), with a significantly shorter bond length of  $1.586 \text{ \AA}$  and correspondingly higher vibrational frequency of  $926 \text{ cm}^{-1}$ . Results at the CCSD(T)/aug-cc-pVTZ level are similar, predicting  $r_e = 1.77 \text{ \AA}$  for the ground state and  $1.612 \text{ \AA}$  for the  $^5\Sigma^+$  excited state, with  $T_e = 2155 \text{ cm}^{-1}$ . These results also agree with the calculations of Miliordos *et al.*<sup>7</sup> Their highest-level results (MRCI, with relativistic correction) predict  $r_e = 1.700 \text{ \AA}$  and vibrational frequency of  $610 \text{ cm}^{-1}$  for the ground state, and  $r_e = 1.601 \text{ \AA}$ , with  $\omega_e = 940 \text{ cm}^{-1}$  for the  $^5\Sigma^+$  excited state, which lies at  $2337 \text{ cm}^{-1}$ . They also recommend a dissociation energy  $D_0 = 230 \text{ kJ/mol}$ . The authors note that the ground state

of  $\text{MnO}^+$  is not well described by a single electronic occupancy (it is multiconfigurational), so it is somewhat surprising that all three methods produce such similar results. Unfortunately, this agreement does not extend to the excited states.

Theoretical potential energy surfaces for the ground state of  $\text{MnO}^+$  and all quintet excited electronic states below  $30,000 \text{ cm}^{-1}$  calculated using TD-DFT (B3LYP/6-311++G(3df,3pd)) are shown in figure 4.1 and those calculated at the EOM-CCSD/aug-cc-pVTZ level are in figure 4.2. The results are quite similar. TD-DFT calculations using the newer CAM-B3LYP and M06 density functionals also give very similar results. The numbers below refer to the EOM-CCSD results. Two fairly intense transitions are predicted in the visible/near UV. The repulsive  $^5\Sigma^-$  state is expected to give a broad feature in the photodissociation spectrum, centered at a vertical energy of  $\sim 23,500 \text{ cm}^{-1}$ . This repulsive state is the highest-energy quintet state calculated by Miliordos *et al.*<sup>7</sup> The excited  $^5\Pi$  state has a very flat potential, with substantially longer bond length ( $2.0 \text{ \AA}$ ) than the ground state. This should lead to a long vibrational progression in the spectrum, starting at  $\sim 26,000 \text{ cm}^{-1}$ . Transitions to these two states have integrated oscillator strengths of  $f = 0.075$  and  $f = 0.044$ , respectively. Comparison of our excited state calculations to the MRCI calculations of Miliordos *et al.* reveals a clear discrepancy: while our calculations reproduce potentials for states that correlate to ground state products, they fail to show potentials that lead to  $\text{Mn}^{+*} (^5\text{S}) + \text{O}$  or  $\text{Mn}^{+*} (^5\text{D}) + \text{O}$ , which lie  $9,473$  and  $\sim 14,500 \text{ cm}^{-1}$  above ground state products, respectively. This is a well-known issue with single-reference calculations.

MRCI calculations have been more challenging; they predict states that correlate to  $\text{Mn}^{+*} (^5\text{D}) + \text{O}$  at some bond lengths, but not at others. Unfortunately, they also make

different predictions regarding the spectrum. The transition to the repulsive  ${}^5\Sigma^-$  state is predicted to be quite weak ( $f = 0.006$ ). There are three  ${}^5\Pi$  states with  $T_e = 24,500 - 28,500$   $\text{cm}^{-1}$ , all with very similar bond lengths to the ground state. Transitions to these states are also weak, with  $f \leq 0.0005$ . These calculations are ongoing, but, in addition to a broad absorption near  $29,000$   $\text{cm}^{-1}$  they predict weak transitions to excited  $\Pi$  states, with little vibrational excitation.

#### 4.4 Photodissociation Spectrum of $\text{MnO}^+$

The photodissociation spectrum of  $\text{MnO}^+$  from  $21,300 - 33,900$   $\text{cm}^{-1}$  was recorded by scanning the photolysis laser energy and monitoring the resultant formation of  $\text{Mn}^+$ . Several such scans were averaged and divided by laser power and parent signal to produce the spectrum shown in figure 4.3. The spectrum is dominated by a single large feature at  $27,240$   $\text{cm}^{-1}$  with no clear vibrational progression. Many far less intense peaks, some with partially resolved rotational structure, can also be seen, mostly at higher energies. There is also a very broad absorption of relatively low intensity underlying the spectrum extending from  $22,800$   $\text{cm}^{-1}$  to  $\sim 27,800$   $\text{cm}^{-1}$ .

The presence of a single dominant peak suggests that the optically excited state has a very similar geometry to that of the ground state. This feature also contains spin-orbit structure, indicative of a transition to an excited state where  $\Lambda > 0$ . The photofragment images on this peak, which will be discussed in detail in the following section, imply that  $\Delta\Lambda = 0$  for the corresponding transition. Taken together, this information confirms that the photofragment signal at  $27,240$   $\text{cm}^{-1}$  is the result of a  ${}^5\Pi \leftarrow {}^5\Pi$  transition. An expansion of this portion of the photodissociation spectrum is shown in

figure 4.4. It is overlaid by a simulated spectrum made in *pGopher*.<sup>13, 14</sup> Because  $\Delta\Lambda=0$  for the transition, the peak spacing only yields the difference in spin-orbit splitting between the two states. Fortunately, Miliordos *et al.* have also calculated a spin-orbit constant ( $A=42\text{ cm}^{-1}$ ) for the  $^5\Pi$  ground state, which the present theory confirms. Using this value, we arrive at a spin-orbit constant of  $A=22\text{ cm}^{-1}$  for the excited  $^5\Pi$  state based on the spectral simulations. The simulated spectrum has a linewidth of  $2\text{ cm}^{-1}$  due to the lifetime of the excited state, which precludes measuring rotational constants.

The smaller peaks in the spectrum are difficult to characterize because the predicted density of electronic states in the region is quite high. They could be due to weak transitions to other quintet states or to spin-forbidden transitions. Miliordos *et al.* predict several  $^3\Pi$  and  $^3\Delta$  states in this energy region, all with similar bond lengths to the ground state. The broad, low intensity dissociation below the dominant  $^5\Pi \leftarrow ^5\Pi$  transition is likely the result of direct excitation to the repulsive  $^5\Sigma^-$  state predicted by theory.

#### 4.5 Images of $\text{Mn}^+$ Fragments

$\text{MnO}^+$  photofragment images were created by tuning the dye laser to several locations in the photodissociation spectrum and gating the imaging detector on the time-of-flight peak corresponding to  $\text{Mn}^+$ . The photofragmentation channels are discussed in terms of the state of the  $\text{Mn}^+$  fragment; the energies remaining after photolysis are not sufficient to electronically excite the neutral O ( $^3\text{P}$ ) cofragment.

The excitation energy of the dominant transition in the photodissociation spectrum is too low to yield electronically excited  $\text{Mn}^+$  products so most of the excess

energy is manifested as translational motion. Indeed, images taken at photon energies ranging from 27,140 – 27,270  $\text{cm}^{-1}$  (the peak of the spectrum) show fairly anisotropic ( $\beta=0.6$ ) product distributions with radii corresponding to ionized fragments with  $\sim 7,000 \text{ cm}^{-1}$  of KER. For example, the velocity distribution shown in figure 4.5 is energetically consistent with formation of  $\text{Mn}^+$  ( $^7\text{S}$ ) photofragments. The higher intensity fragment signal is located at the north and south poles of the image. This vertical anisotropy indicates that the orientation of the transition dipole moment is parallel with the electric polarization vector of the photolysis laser, consistent with the  $^5\Pi \leftarrow ^5\Pi$  transition predicted by the calculations. The observed anisotropy parameter is positive ( $\beta=0.6$ ), confirming a parallel electronic transition ( $\Delta\Lambda=0$ ). However, it is below the limiting value ( $\beta=2.0$ ), indicating that the molecular electronic state being accessed is not directly dissociative, but is still shorter lived than a rotational period. This suggests that the predissociative electronic state being excited in this region likely couples to a nearby repulsive state, which yields ground state photofragments.

In order to more precisely measure the bond dissociation energy of  $\text{MnO}^+$ , it is advantageous to record images that are energetically close to a product threshold, where photofragments have little kinetic energy (as shown in Chapter 3). The benefit of imaging photofragments with low KER is the better energy resolution; less extrapolation is required to calculate  $D_0$ . Since no fragmentation is observed at the lowest energies in the photodissociation spectrum, several images were recorded in the higher energy region ( $> 30,000 \text{ cm}^{-1}$ ), near the onset of  $\text{Mn}^{+*}$  ( $^5\text{S}$ ) production. The image in figure 4.6 reveals the production of both ground state  $\text{Mn}^+$  ( $^7\text{S}$ ) fragments (outer ring) as well as the higher energy  $\text{Mn}^{+*}$  ( $^5\text{S}$ ) channel (inner). The images recorded in this region are isotropic for

each fragment channel, indicating that the photodissociation process takes longer than the rotational period of the parent ion in both cases.

The bond dissociation energy of  $\text{MnO}^+$  is determined by analyzing the KER of images recorded at multiple wavelengths. The total KER from each of the energetically accessible dissociation pathways is plotted against the photon energy at which the corresponding image was recorded (Figure 4.7). The full conservation of energy method that is used to calculate the bond dissociation energy is described in detail in Chapter 2.2.5. Briefly though, the bond strength ( $D_0 = 242 \pm 5$  kJ/mol) is determined by subtracting the total internal energy of the relevant fragments<sup>15</sup> from the y-intercepts of the linear trendlines. This value is compared with other published experimental and theoretical values in table 4.1. The  $D_0$  reported here is in good agreement with the original ion beam measurement of Armentrout *et al.*<sup>8</sup> As for theory, even the highest level *ab initio* results available<sup>7</sup> underestimate the bond strength by 10 -15 kJ/mol, while DFT methods tend to overestimate it in many cases.<sup>6, 16</sup>

$\text{MnO}^+$  is a surprising challenge for theoretical assessment, and the success of our own calculations is mixed. The broad absorption predicted to occur to the repulsive  $^5\Sigma^-$  potential is present in the photodissociation spectrum. A single strong transition, identified as  $^5\Pi \leftarrow ^5\Pi$ , is also seen in the spectrum. The intensity of this transition agrees with TD-DFT and EOM-CCSD calculations presented here. However, they both predict a long vibrational progression which is not experimentally observed. The MRCI method predicts excited  $^5\Pi$  states with similar geometries to the ground state, and hence, no vibrational progression, but the transitions to these states are predicted to be quite weak.

Overall though, the experimental and theoretical results presented here help to identify where the strengths and weaknesses lie in each method.

## 4.6 Conclusions

Photofragment spectroscopy and ion imaging from 21,300 – 33,900  $\text{cm}^{-1}$  has been used to probe the bond dissociation energy and dynamics of  $\text{MnO}^+$ . The experimental results are compared to electronic structure calculations performed at the TD-DFT, EOM-CCSD, and MRCI levels and to theoretical results available in the published literature. The photodissociation spectrum displays a dominant feature centered at 27,200  $\text{cm}^{-1}$ . The lack of a vibrational progression indicates that the excited state has a similar bond length to the ground state. The presence of spin-orbit structure within this peak, along with the vertical anisotropy of the corresponding photofragments indicate that the fragments result from a predissociative  ${}^5\Pi \leftarrow {}^5\Pi$  transition. This finding experimentally confirms the expected identity of the ground state ( ${}^5\Pi$ ) of  $\text{MnO}^+$  and, using the agreed upon theoretical spin-orbit constant for the ground state, provides a spin-orbit constant ( $A = 22 \text{ cm}^{-1}$ ) for the  ${}^5\Pi$  excited state. Other features and progressions in the photodissociation spectrum are much less intense, irregular, and difficult to precisely assign to theoretical electronic potentials given the high density of electronic states in the region. Images at energies above 30,000  $\text{cm}^{-1}$  indicate the opening of a new photodissociation channel corresponding to  $\text{Mn}^{+*} ({}^5\text{S}) + \text{O} ({}^3\text{P})$  fragments, which quickly dominates the  $\text{Mn}^+ ({}^7\text{S})$  ground state pathway. By photolyzing  $\text{MnO}^+$  at known energies and measuring the corresponding kinetic energy releases from several photofragment images, we obtain the bond dissociation energy of  $\text{MnO}^+$  ( $D_0 = 242 \pm 5 \text{ kJ/mol}$ ).

## 4.7 References

1. J. Roithova and D. Schroder, Chem. Rev. **110**, 1170-1211 (2010).
2. K. A. Zemski, D. R. Justes and A. W. Castleman, J. Phys. Chem. B **106**, 6136-6148 (2002).
3. M. F. Ryan, A. Fiedler, D. Schröder and H. Schwarz, J. Am. Chem. Soc. **117**, 2033-2040 (1995).
4. K. Yoshizawa, Y. Shiota and T. Yamabe, J. Am. Chem. Soc. **120**, 564-572 (1998).
5. Y. Shiota and K. Yoshizawa, J. Am. Chem. Soc. **122**, 12317-12326 (2000).
6. C. W. Bauschlicher and G. L. Gutsev, Theor. Chem. Acc. **107**, 309-312 (2002).
7. E. Miliordos and A. Mavridis, J. Phys. Chem. A **114**, 8536-8572 (2010).
8. P. B. Armentrout, L. F. Halle and J. L. Beauchamp, J. Chem. Phys. **76**, 2449-2457 (1982).
9. E. R. Fisher, J. L. Elkind, D. E. Clemmer, R. Georgiadis, S. K. Loh, N. Aristov, L. S. Sunderlin and P. B. Armentrout, J. Chem. Phys. **93**, 2676-2691 (1990).
10. *Gaussian 09*, M. J. Frisch, G. W. Trucks, H. B. Schlegel, G. E. Scuseria, M. A. Robb, J. R. Cheeseman, G. Scalmani, V. Barone, B. Mennucci and G. A. Petersson, (Gaussian, Inc., Wallingford, CT, Pittsburgh PA, 2010).
11. *MOLPRO, version 2015.1, a package of ab initio programs*, H. J. Werner, P. J. Knowles, G. Knizia, F. R. Manby, M. Schutz and others.
12. H. J. Werner, P. J. Knowles, G. Knizia, F. R. Manby and M. Schutz, WIREs Comput. Mol. Sci **2**, 242-253 (2012).
13. C. M. Western, J. Quant. Spec. Radiat. Transfer **186**, 221-242 (2016).
14. *pGopher, A Program for Simulating Rotational, Vibrational and Electronic Spectra*, C. M. Western, (University of Bristol, 2015).
15. A. Kramida, Y. Ralchenko, J. Reader and NIST ASD Team. (2018). *NIST Atomic Spectra Database (Version 5.5.2)*, Available: <http://physics.nist.gov/asd>. (National Institute of Standards and Technology, Gaithersburg, MD)
16. Y. Nakao, K. Hirao and T. Taketsugu, J. Chem. Phys. **114**, 7935-7940 (2001).

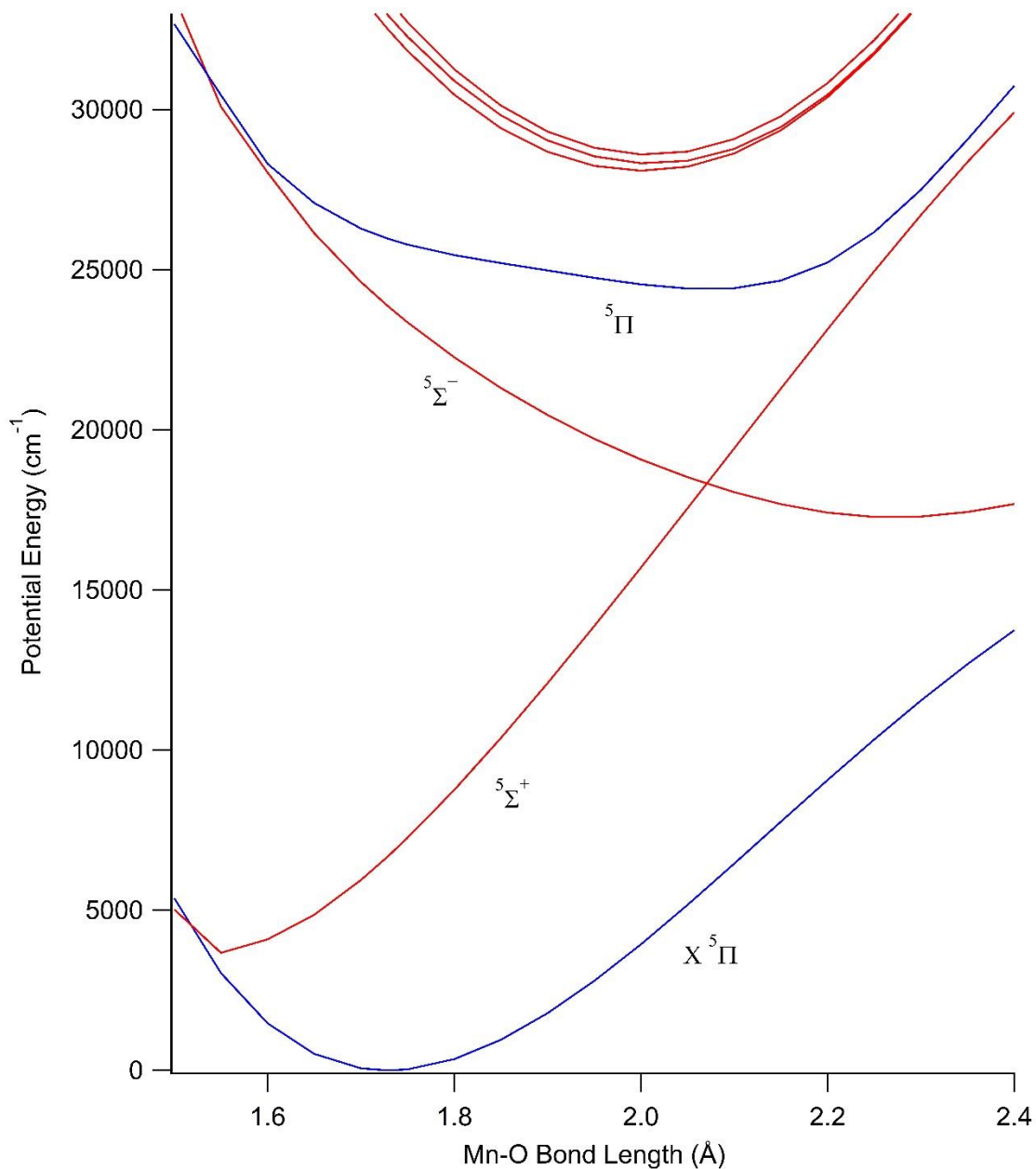


Figure 4.1. Potential energy curves for quintet states of MnO<sup>+</sup> calculated using TD-DFT with the B3LYP functional and 6-311++G(3df,3pd) basis set. Red lines represent excited states reached through perpendicular ( $\Delta\Lambda = \pm 1$ ) transitions from the ground state (X <sup>5</sup>Π). A transition to the blue curve is parallel ( $\Delta\Lambda = 0$ ).

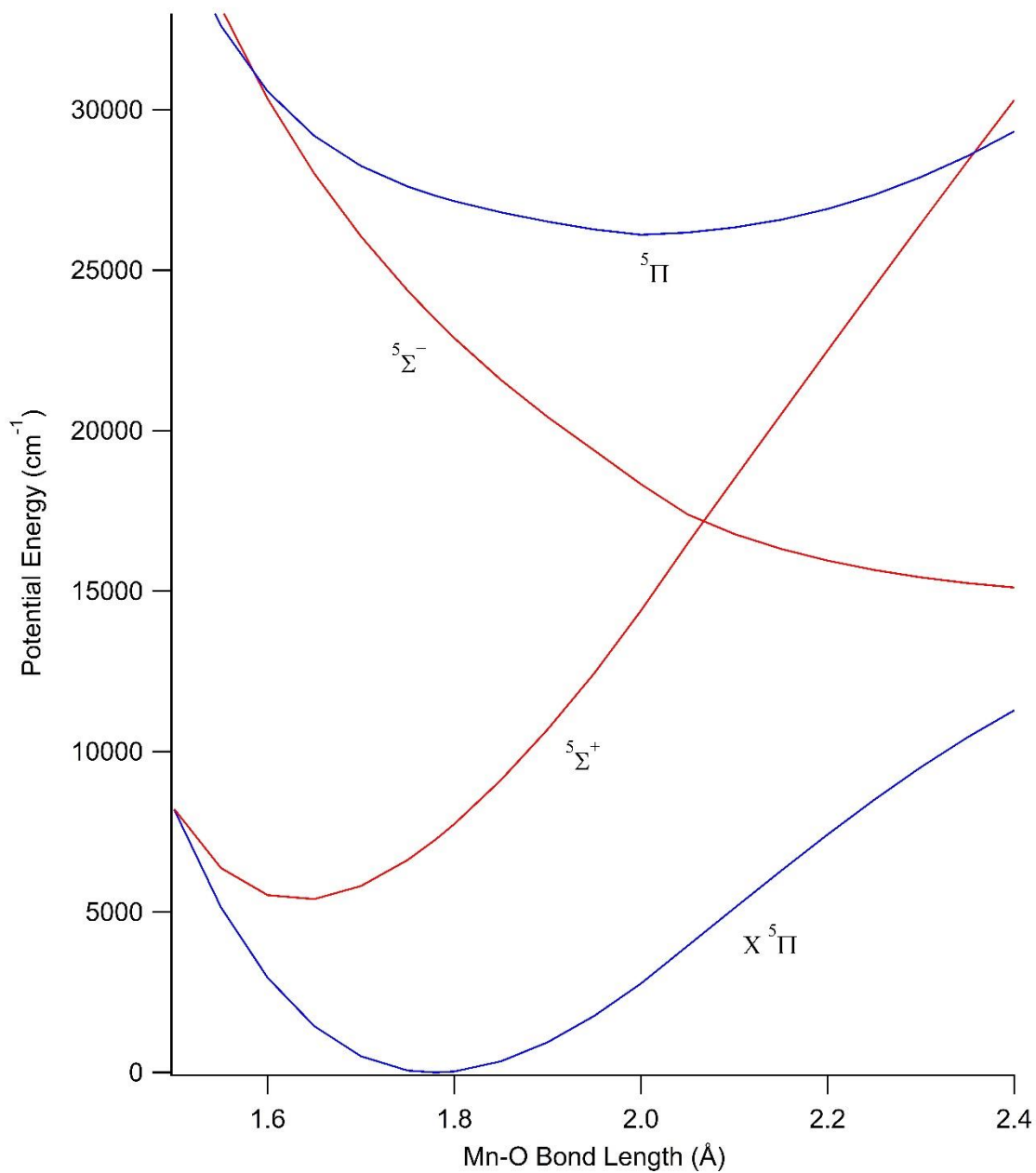


Figure 4.2. Potential energy curves for quintet states of  $\text{MnO}^+$  calculated using EOM-CCSD with the aug-cc-pVTZ basis set. Red lines represent excited states reached through perpendicular ( $\Delta\Lambda = \pm 1$ ) transitions from the ground state ( $X^5\Pi$ ). A transition to the blue curve is parallel ( $\Delta\Lambda = 0$ ).

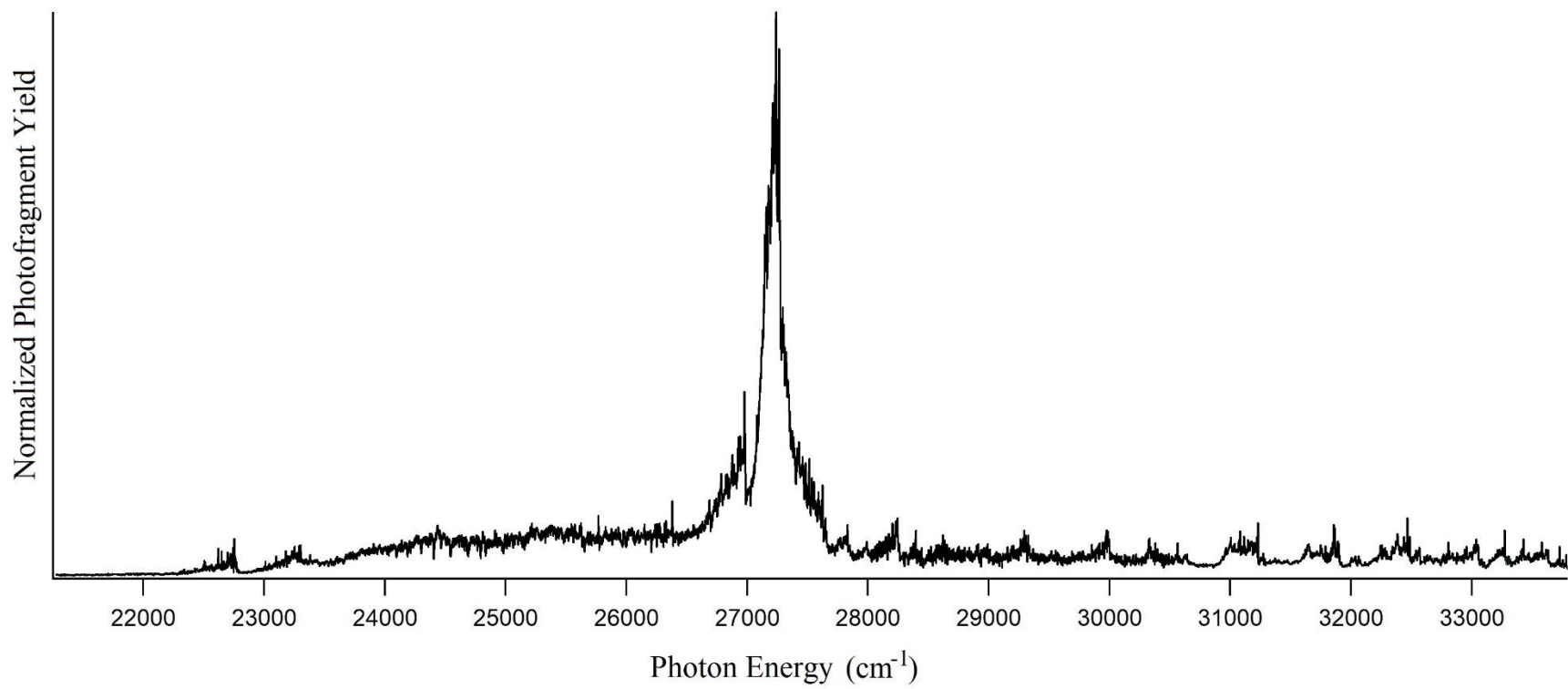


Figure 4.3. Photodissociation spectrum of MnO<sup>+</sup> from 21,300 – 33,900 cm<sup>-1</sup>.

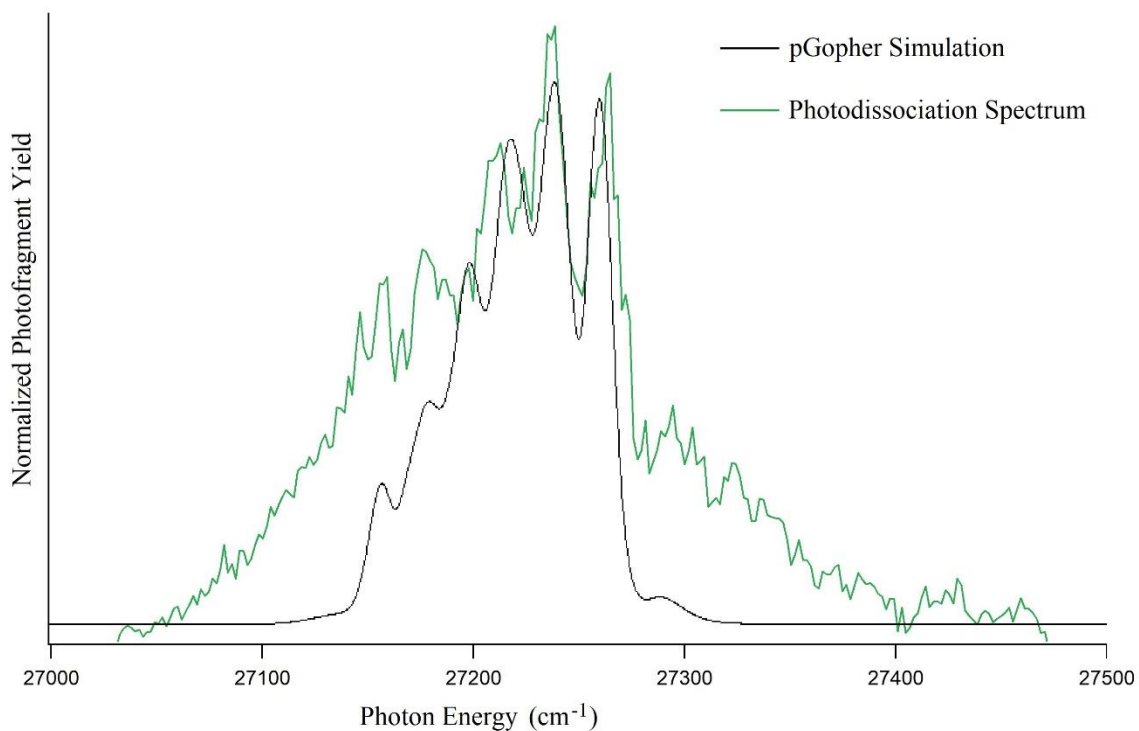


Figure 4.4. Photodissociation spectrum of  $\text{MnO}^+$  from 27,000 – 27,500  $\text{cm}^{-1}$ . The simulated spectrum was made in pGopher assuming a ( ${}^5\Pi \leftarrow X {}^5\Pi$ ) transition between states of the same geometry and where  $A(X {}^5\Pi) = 42 \text{ cm}^{-1}$  and  $A({}^5\Pi) = 22 \text{ cm}^{-1}$ . The simulated linewidth is  $2 \text{ cm}^{-1}$ .

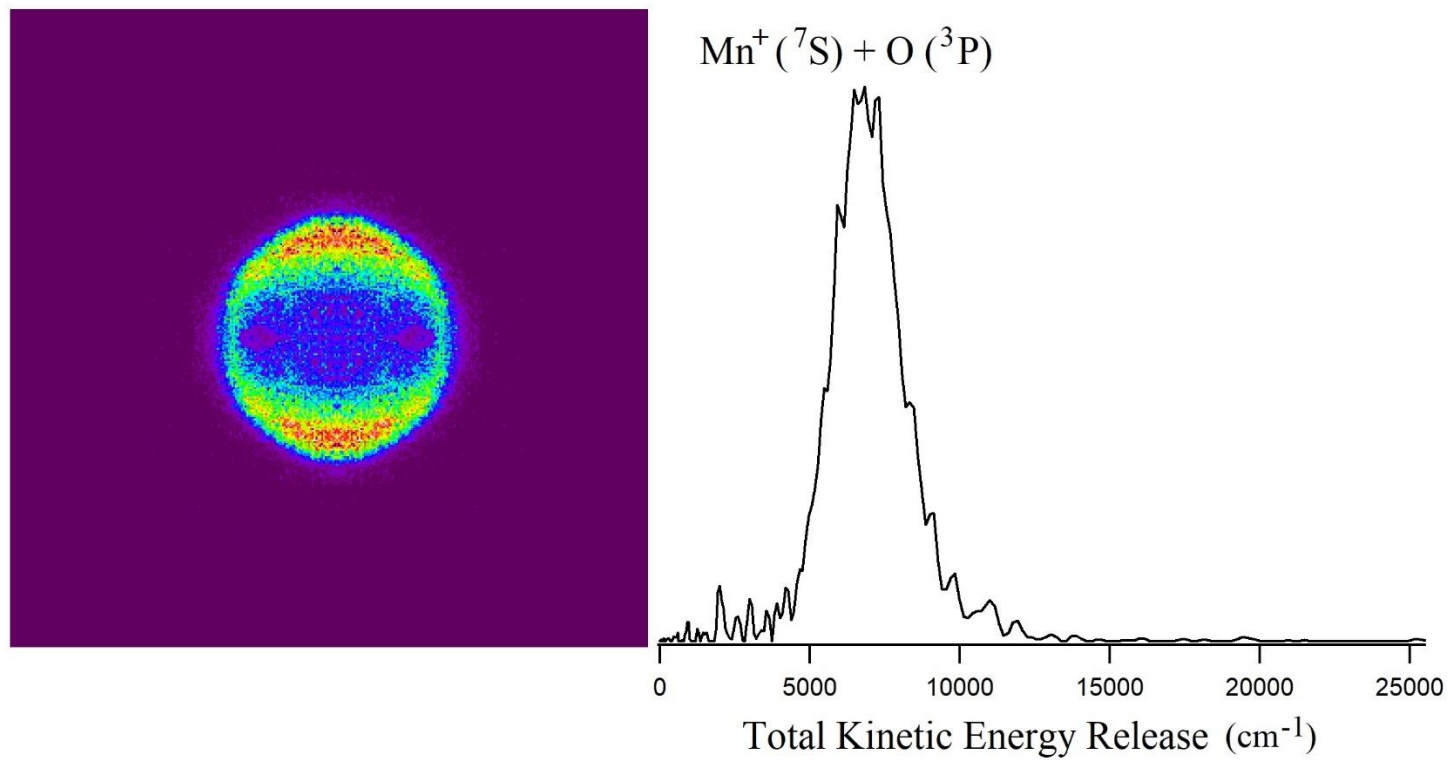


Figure 4.5. Photofragment image of  $\text{Mn}^+$  made by dissociating  $\text{MnO}^+$  at  $27,278 \text{ cm}^{-1}$  and the corresponding velocity distribution converted to total kinetic energy release. The image shown has been top/bottom and left/right symmetrized. Laser polarization is vertical.

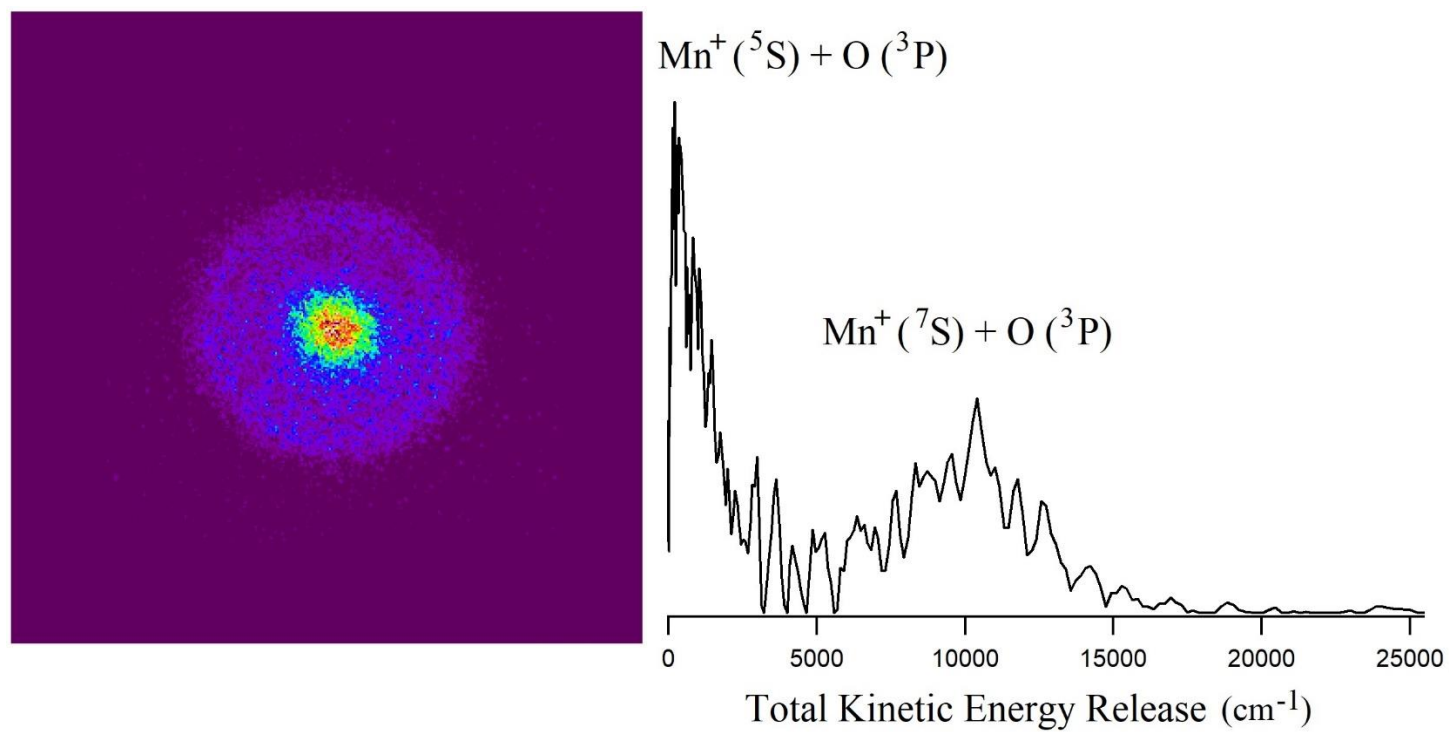


Figure 4.6. Photofragment image of  $\text{Mn}^+$  made by dissociating  $\text{MnO}^+$  at  $30,488 \text{ cm}^{-1}$  and the corresponding velocity distribution converted to total kinetic energy release. Laser polarization is vertical.

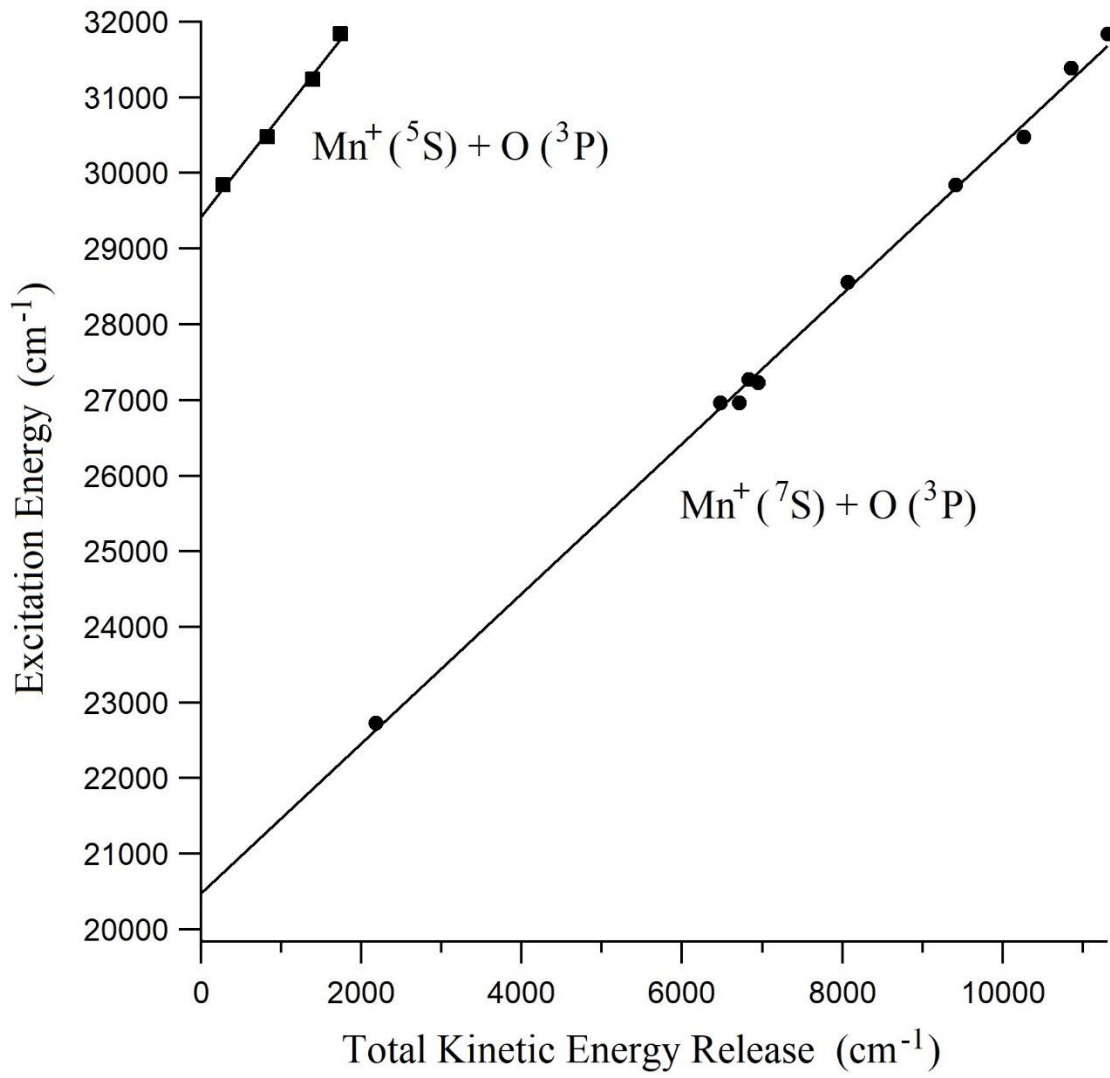


Figure 4.7. Plot of excitation energy versus total kinetic energy release for several images of  $\text{Mn}^+$  products resulting from photodissociation of cold  $\text{MnO}^+$ . The bond dissociation energy ( $D_0$ ) of  $\text{MnO}^+$  is obtained by subtracting the known threshold energies from each y-intercept of the linear fits.

Table 4.1. Experimental and theoretical bond dissociation energies ( $D_0$ ) of  $\text{MnO}^+$  ( $^5\Pi$ ).

$D_0$ of $\text{MnO}^+$ (kJ/mol)	Experiment
$239 \pm 10$	Ion Beam <sup>8</sup>
$285 \pm 13$	Ion Beam <sup>9</sup>
$242 \pm 5$	VMI (present study)
Theory	
230 <sup>a</sup>	C-MRCI+DKH2+Q <sup>7</sup>
233	MRMP <sup>16</sup>
225	IC-MRCI+Q <sup>6</sup>
255	B3LYP <sup>6</sup>
251	B3LYP <sup>16</sup>
273 <sup>b</sup>	CASPT2D <sup>3</sup>

<sup>a</sup> The  $D_e$  obtained was converted to  $D_0$  by subtracting a zero-point energy of 3.6 kJ/mol.

<sup>b</sup> The  $D_0$  obtained assumes a  $^5\Sigma^+$  ground state and not the  $^5\Pi$  ground state reported here.

## CHAPTER 5

### CONCLUSIONS AND FUTURE DIRECTIONS

#### 5.1 Conclusions

In summary, a new instrument is demonstrated that is capable of performing velocity map imaging (VMI) experiments on the photofragments of cold, mass selected ions in a fast ion beam. The ions are produced in a dual-purpose laser ablation/discharge source and collisionally thermalized in a refrigerated ( $\geq 7$  K) ion trap prior to spectroscopy and imaging. The current resolution of the experiment ( $\Delta v / v = 7.6\%$ ) and the factors that contribute to it have been discussed in detail after analyzing the radial and angular distributions of a number of photolysis products. Photofragment imaging of  $\text{N}_2\text{O}^+$  indicates that photodissociation at 323 nm results in rotationally hot  $\text{NO}^+$  fragments with a very specific vibrational population ( $v = 5$ ). Images of  $\text{N}_2\text{O}^+$  photolysis at 310 nm demonstrate competition between a spin-forbidden ground state product channel  $\text{N}(^4\text{S}) + \text{NO}^+$  and a spin-allowed excited state pathway  $\text{N}^*(^2\text{D}) + \text{NO}^+$ , a finding that supports the published literature.

The photodissociation dynamics and electronic state structure of  $\text{Al}_2^+$  have been investigated by photodissociation spectroscopy and photofragment imaging in the 20,000 – 23,800  $\text{cm}^{-1}$  and 38,500 – 42,000  $\text{cm}^{-1}$  regions. These experiments are compared to theory at the EOM-CCSD(full)/(aug-cc-pVQZ) and MRCI-F12/(aug-cc-pVTZ) levels in order to further elucidate the complex excited state structure of the aluminum dimer cation. As predicted, the directly dissociative  $\text{C } ^2\Sigma_u^+ \leftarrow \text{X } ^2\Sigma_g^+$  transition yields purely ground state photoproducts  $\text{Al}(^2\text{P}^\circ) + \text{Al}^+(^1\text{S})$  with limiting parallel anisotropy ( $\beta=2$ ) and significant kinetic energy release. The theory predicts that the  $\text{G } ^2\Sigma_u^+$  potential energy

surface has two minima with an avoided crossing near the vertical excitation from the ground state. This behavior is manifested in the extremely anharmonic photodissociation spectrum observed in the corresponding spectral region. Analysis of photodissociation spectra at various temperatures gives  $\nu_0 = 172 \text{ cm}^{-1}$  for the ground state ( $X \ ^2\Sigma^+_g$ ) and an average vibrational spacing of  $170 \text{ cm}^{-1}$  for the excited state ( $G \ ^2\Sigma^+_u$ ). Photofragment images reveal that Al ( $^4P$ ) products immediately dominate the lower energy Al ( $^2P^\circ$ ) and Al ( $^2S$ ) channels once the high energy pathway is energetically accessible. The calculations suggest that the  $G \ ^2\Sigma^+_u$  state eventually correlates adiabatically to Al ( $^2S$ ) products after a wide barrier at higher bond lengths. Thus, it is expected that the spin-allowed Al ( $^2S$ ) channel will be favored over the Al ( $^4P$ ) pathway once the excitation energy surpasses the barrier height. The radial distributions of Al<sup>+</sup> fragments give an improved experimental value for the bond dissociation energy of Al<sub>2</sub><sup>+</sup> ( $D_0 = 136.6 \pm 1.8 \text{ kJ/mol}$ ). The improved uncertainty of this value over that obtained from the  $C \ ^2\Sigma^+_u \leftarrow X \ ^2\Sigma^+_g$  transition ( $D_0 = 138 \pm 5 \text{ kJ/mol}$ ) highlights the improved resolution achieved from imaging very close to a corresponding photoproduct threshold (low fragment kinetic energy). The surprisingly low photofragment yield from the  $G \ ^2\Sigma^+_u \leftarrow X \ ^2\Sigma^+_g$  transition is explained by a likely competition between relatively fast fluorescence and the previously discussed non-radiative dissociation pathways.

Photofragment spectroscopy and ion imaging from  $21,300 - 33,900 \text{ cm}^{-1}$  has been used to elucidate the bond strength and photodissociation dynamics of MnO<sup>+</sup>. Experimental results are compared to electronic structure calculations performed at the TD-DFT, EOM-CCSD, and MRCI levels and to theory available in the published literature. Our calculations predict a weak optical transition from the  $^5\Pi$  ground state to a

repulsive  $^5\Sigma^-$  excited state. Fragmentation from this transition is observed in the photodissociation spectrum over a broad region beginning at  $22,800\text{ cm}^{-1}$ . The theoretical methods also predict a transition to a bound  $^5\Pi$  state, though they tend to disagree on the oscillator strength and exact geometry of the excited state. The photofragment spectrum displays a dominant feature with spin-orbit structure centered at  $27,200\text{ cm}^{-1}$ . This structure, along with the vertically anisotropic photofragments, experimentally confirms the  $^5\Pi \leftarrow ^5\Pi$  transition predicted by theory. The intensity of this transition agrees with TD-DFT and EOM-CCSD calculations. However, they both predict a long vibrational progression not seen in the spectrum. The MRCI method predicts that the  $^5\Pi$  state has a much more similar geometry to the ground state, but the transition is thought to be weaker. The spin-orbit constant ( $A = 22\text{ cm}^{-1}$ ) of the optically excited  $^5\Pi$  state is determined from pGopher simulations using the aforementioned spin-orbit structure and the previously calculated spin-orbit constant of the ground state. The other less intense features and progressions in the photodissociation spectrum of  $\text{MnO}^+$  are irregular and difficult to identify given the high predicted density of states in the region. Photofragment images recorded at excitation energies above  $30,000\text{ cm}^{-1}$  indicate the presence of a higher energy photoproduct channel corresponding to  $\text{Mn}^{+*} (^5\text{S}) + \text{O} (^3\text{P})$  fragments, which quickly dominates the  $\text{Mn}^+ (^7\text{S})$  ground state pathway. By photolyzing  $\text{MnO}^+$  at several energies and measuring the kinetic energy releases from several corresponding photofragment images, we obtain a new bond dissociation energy for  $\text{MnO}^+$  ( $D_0 = 242 \pm 5\text{ kJ/mol}$ ). This value refines the previously published experimental and theoretical results.

## 5.2 Future Directions

The metal-containing ions presented in this study were chosen as fundamental examples of computationally difficult systems that also lack a solid base of experimental benchmarks. They represent seemingly simple diatomic systems that are well suited for study using the newly constructed fast ion photofragment imaging mass spectrometer. There are many other metal dimer and metal oxide ions that fall into the same vein. Not to mention the numerous other small ligand/metal combinations, whose experimental photochemical properties need to be understood as we advance toward more and more accurate theoretical models of metal chemistry. It is important that future photofragment imaging work continue to focus on the lesser studied metal-containing species, not only on metal dimers and oxides, but also on slightly larger metal clusters and ligated metal centers.

There are several promising species that are suggested for immediate future study. The nickel oxide cation ( $\text{NiO}^+$ ), like  $\text{MnO}^+$ , is known to exothermically activate C-H bonds. However,  $\text{NiO}^+$  has proven to be a far more efficient catalyst for the methane to methanol conversion process.  $\text{NiO}^+$  is virtually 100% selective in producing the more desirable methanol product from its reaction with methane, orders of magnitude better than  $\text{MnO}^+$ . In exchange, it is only about half as reactive as  $\text{MnO}^+$ . There are also fairly large discrepancies in the few available experimentally determined bond dissociation energies of  $\text{NiO}^+$ . Understanding the photodissociation dynamics of  $\text{NiO}^+$  would also be an important part of clarifying its promising catalytic behavior. The nickel oxide cation is therefore a logical next step for photofragment imaging. The production of  $\text{NiO}^+$  should be facile; ablating a nickel disc in the presence of an oxidizing agent like  $\text{N}_2\text{O}$  should be

sufficient to generate plenty of parent ions. It also helps that  $\text{Ni}^+$  has well separated spin-orbit states, which should be resolvable even after combining with each J-state in the oxygen cofragment.

In general, there are several ligated transition metal species that represent steps in the process of catalytic activation. The bond strengths of many metal-carbenes and metal-carbonyls have not been accurately measured and they would be good candidates for photofragment imaging studies. Those species with few low-lying electronic states are traditionally troublesome for study via thermodynamic dissociation onset spectroscopy. They are, however, good candidates for photofragment imaging given that their product states are sufficiently separated.

Finally, it is suggested that photofragment imaging studies continue on metal-containing systems that are analogous to the aluminum dimer cation presented here. Other group 13 metal dimers and trimers have been extensively theoretically studied as they relate to the chemical trends of increasing cluster size. However, they also suffer from lack of experimental benchmarks. These clusters are excellent fits for photofragment imaging studies because transitions involving their few valence electrons are relatively easy to identify and, in many cases, will result in photodissociation to well separated fragment states. The small and intermediate sized clusters have been observed to occasionally dissociate by ejecting a single charged metallic fragment, while the bulkier cofragment remains neutral. Such cases are examples of systems with outstanding kinematics, and would result in significantly improved energy resolution at the imaging detector.

Ultimately, there are inherent resolution limitations associated with imaging the photofragments of ions with a large number of degrees of freedom. However, there are still many things that are poorly understood about bonding between metallic elements in smaller molecules and ions. Imaging the photofragments of fast ions beams should continue to be a valuable technique in the continuing quest to elucidate these most fundamental chemical interactions.

## BIBLIOGRAPHY

*Gas-Phase Cluster Ions*, edited by M. T. Bowers, M. F. Jarrold and A. J. Stock, Special Issue. Int. J. Mass. Spectrom. Ion. Proc., (Elsevier, Amsterdam, 1990).

*Imaging in Chemical Dynamics*, edited by A. G. Suits and R. E. Continetti, ACS Symposium Series 770, (American Chemical Society, Washington DC, 2000).

*Imaging in Molecular Dynamics: Technology and Applications*, edited by B. J. Whitaker, (Cambridge University Press, New York, 2003).

S. Abed, M. Broyer, M. Carre, M. L. Gaillard and M. Larzilliere, Chem. Phys. **74**, 97-112 (1983).

P. B. Armentrout, Annu. Rev. Phys. Chem. **52**, 423-461 (2001).

P. B. Armentrout, L. F. Halle and J. L. Beauchamp, J. Chem. Phys. **76**, 2449-2457 (1982).

M. N. R. Ashfold, N. H. Nahler, A. J. Orr-Ewing, O. P. J. Vieuxmaire, R. L. Toomes, T. N. Kitsopoulos, I. A. Garcia, D. A. Chestakov, S. M. Wu and D. H. Parker, Phys. Chem. Chem. Phys. **8**, 26-53 (2006).

C. W. Bauschlicher and G. L. Gutsev, Theor. Chem. Acc. **107**, 309-312 (2002).

C. W. Bauschlicher Jr., L. A. Barnes and P. R. Taylor, J. Phys. Chem. **93**, 2932-2935 (1989).

M. Beckert, S. J. Greaves and M. N. R. Ashfold, Phys. Chem. Chem. Phys. **5**, 308-314 (2003).

M. Brack, Rev. Mod. Phys. **65**, 677-732 (1993).

M. F. Cai, C. C. Carter, T. A. Miller and V. E. Bondybey, Chem. Phys. **155**, 233-245 (1991).

J. H. Callomon and F. Creutzberg, Philos. Trans. Roy. Soc. London, Ser. A **277**, 158-189 (1974).

C. J. Cassady and B. S. Freiser, J. Am. Chem. Soc. **106**, 6176-6179 (1984).

G. Chambaud, H. Gritli, P. Rosmus, H. J. Werner and P. J. Knowles, Mol. Phys. **98**, 1793-1802 (2000).

D. W. Chandler and P. L. Houston, J. Chem. Phys. **87**, 1445-1447 (1987).

B. Y. Chang, R. C. Hoetzlein, J. A. Mueller, J. D. Geiser and P. L. Houston, Rev. Sci. Instrum. **69**, 1665-1670 (1998).

R. E. Continetti, D. R. Cyr and D. M. Neumark, Rev. Sci. Instrum. **63**, 1840-1841 (1992).

- D. A. Dahl, *Int. J. Mass Spectrom.* **200**, 3-25 (2000).
- B. B. Dangi and K. M. Ervin, *J. Mass Spectrom.* **47**, 41-48 (2012).
- W. A. Deheer, *Rev. Mod. Phys.* **65**, 611-676 (1993).
- V. Dribinski, A. Ossadtchi, V. A. Mandelshtam and H. Reisler, *Rev. Sci. Instrum.* **73**, 2634-2642 (2002).
- A. T. J. B. Eppink and D. H. Parker, *Rev. Sci. Instrum.* **68**, 3477-3484 (1997).
- E. R. Fisher, J. L. Elkind, D. E. Clemmer, R. Georgiadis, S. K. Loh, N. Aristov, L. S. Sunderlin and P. B. Armentrout, *J. Chem. Phys.* **93**, 2676-2691 (1990).
- Gaussian 09*, M. J. Frisch, G. W. Trucks, H. B. Schlegel, G. E. Scuseria, M. A. Robb, J. R. Cheeseman, G. Scalmani, V. Barone, B. Mennucci and G. A. Petersson, (Gaussian, Inc., Wallingford, CT, Pittsburgh PA, 2010).
- Z. W. Fu, G. W. Lemire, G. A. Bishea and M. D. Morse, *J. Chem. Phys.* **93**, 8420-8441 (1990).
- G. A. Garcia, L. Nahon and I. Powis, *Rev. Sci. Instrum.* **75**, 4989-4996 (2004).
- C. R. Gebhardt, T. P. Rakitzis, P. C. Samartzis, V. Ladopoulos and T. N. Kitsopoulos, *Rev. Sci. Instrum.* **72**, 3848-3853 (2001).
- S. Han, H. Hettema and D. R. Yarkony, *J. Chem. Phys.* **102**, 1955-1964 (1995).
- L. Hanley, S. A. Ruatta and S. L. Anderson, *J. Chem. Phys.* **87**, 260-268 (1987).
- J. E. Harrington and J. C. Weisshaar, *J. Chem. Phys.* **93**, 854-855 (1990).
- W. L. P. III, C. Copeland, A. Kocak, Z. Sallase and R. B. Metz, *J. Chem. Phys.* **141**, 204305 (2014).
- O. Ingólfsson, H. Takeo and S. Nonose, *J. Chem. Phys.* **110**, 4382-4393 (1999).
- Y. Y. Jau, F. M. Benito, H. Partner and P. D. D. Schwindt, *Rev. Sci. Instrum.* **82**, 023118 (2011).
- R. M. Jones, D. Gerlich and S. L. Anderson, *Rev. Sci. Instrum.* **68**, 3357-3362 (1997).
- M. Z. Kamrath, R. A. Relph, T. L. Guasco, C. M. Leavitt and M. A. Johnson, *Int. J. Mass Spectrom.* **300**, 91-98 (2011).
- M. H. Kim, B. D. Leskiw and A. G. Suits, *J. Phys. Chem. A* **109**, 7839-7842 (2005).

V. O. Kiohara, E. F. V. Carvalho, C. W. A. Paschoal, F. B. C. Machado and O. Roberto-Neto, *Chem. Phys. Lett.* **568**, 42-48 (2013).

A. Kocak, G. Austein-Miller, W. L. Pearson III, G. Altinay and R. B. Metz, *J. Phys. Chem. A* **117**, 1254-1264 (2013).

A. Kramida, Y. Ralchenko, J. Reader and NIST ASD Team. (2018). *NIST Atomic Spectra Database (Version 5.5.2)*, Available: <http://physics.nist.gov/asd>. (National Institute of Standards and Technology, Gaithersburg, MD)

J. Lerme, S. Abed, M. Larzilliere, R. A. Holt and M. Carre, *J. Chem. Phys.* **84**, 2167-2179 (1986).

W. Li, S. D. Chambreau, S. A. Lahankar and A. G. Suits, *Rev. Sci. Instrum.* **76**, 063106 (2005).

J. A. Maner, D. T. Mauney and M. A. Duncan, *J. Phys. Chem. Lett.* **6**, 4493-4498 (2015).

J. A. Maner, D. T. Mauney and M. A. Duncan, *Chem. Phys. Lett.* **671**, 182-185 (2017).

S. Manzhos and H.-P. Looock, *Comput. Phys. Commun.* **154**, 76-87 (2003).

D. J. Matthew, E. Tieu and M. D. Morse, *J. Chem. Phys.* **146**, 10 (2017).

R. B. Metz, *Int. J. Mass Spectrom.* **235**, 131-143 (2004).

R. B. Metz, *Int. Rev. Phys. Chem.* **23**, 79-108 (2004).

E. Miliordos and A. Mavridis, *J. Phys. Chem. A* **114**, 8536-8572 (2010).

N. H. Nahler, O. P. J. Vieuxmaire, J. R. Jones, M. N. R. Ashfold, A. T. J. B. Eppink, A. M. Coriou and D. H. Parker, *J. Phys. Chem. A* **108**, 8077-8083 (2004).

Y. Nakao, K. Hirao and T. Taketsugu, *J. Chem. Phys.* **114**, 7935-7940 (2001).

D. M. Neumark, *J. Phys. Chem. A* **112**, 13287-13301 (2008).

K. Okutsu, Y. Nakashima, K. Yamazaki, K. Fujimoto, M. Nakano, K. Ohshimo and F. Misaizu, *Rev. Sci. Instrum.* **88**, 053105 (2017).

I. S. Parry, A. C. Hermes, A. Kartouzian and S. R. Mackenzie, *Phys. Chem. Chem. Phys.* **16**, 458-466 (2014).

L. A. Posey, M. J. DeLuca and M. A. Johnson, *Chem. Phys. Lett.* **131**, 170-174 (1986).

D. R. A. Ranatunga and B. S. Freiser, *Chem. Phys. Lett.* **233**, 319-323 (1994).

M. Richardviard, O. Atabek, O. Dutuit and P. M. Guyon, *J. Chem. Phys.* **93**, 8881-8892 (1990).

- J. Roithova and D. Schroder, *Chem. Rev.* **110**, 1170-1211 (2010).
- M. Rosi, C. W. Bauschlicher Jr. and S. R. Langhoff, *Chem. Phys.* **151**, 1-9 (1991).
- M. F. Ryan, A. Fiedler, D. Schröder and H. Schwarz, *J. Am. Chem. Soc.* **117**, 2033-2040 (1995).
- A. G. Sage, T. A. A. Oliver, R. N. Dixon and M. N. R. Ashfold, *Mol. Phys.* **108**, 945-955 (2010).
- A. Sanov and R. Mabbs, *Int. Rev. Phys. Chem.* **27**, 53-85 (2008).
- W. A. Saunders, P. Fayet and L. Woste, *Phys. Rev. A* **39**, 4400-4405 (1989).
- J. J. Scherer, J. B. Paul and R. J. Saykally, *Chem. Phys. Lett.* **242**, 395-400 (1995).
- A. Sevy, J. J. Sorensen, T. D. Persinger, J. A. Franchina, E. L. Johnson and M. D. Morse, *J. Chem. Phys.* **147**, 8 (2017).
- Y. Shiota and K. Yoshizawa, *J. Am. Chem. Soc.* **122**, 12317-12326 (2000).
- P. C. Singh, L. Shen, J. Zhou, H. B. Schlegel and A. G. Suits, *Astrophys. J.* **710**, 112-116 (2010).
- C. A. Stearns and F. J. Kohl, *High Temp. Sci.* **5**, 113-127 (1973).
- K. K. Sunil and K. D. Jordan, *J. Phys. Chem.* **92**, 2774-2781 (1988).
- X. Tang, M. Niu, X. Zhou, S. Liu, F. Liu, X. Shan and L. Sheng, *J. Chem. Phys.* **134**, 054312 (2011).
- H. L. Tao, L. Shen, M. H. Kim, A. G. Suits and T. J. Martinez, *J. Chem. Phys.* **134**, 054313 (2011).
- D. Townsend, M. P. Minitti and A. G. Suits, *Rev. Sci. Instrum.* **74**, 2530-2539 (2003).
- E. C. Tyo and S. Vajda, *Nat. Nanotechnol.* **10**, 577-588 (2015).
- S. E. Waller, J. E. Mann and C. C. Jarrold, *J. Phys. Chem. A* **117**, 1765-1772 (2013).
- H. Wang, X. Zhou, S. Liu, B. Jiang, D. Dai and X. Yang, *J. Chem. Phys.* **132**, 244309 (2010).
- X. B. Wang and L. S. Wang, *Rev. Sci. Instrum.* **79**, 073108 (2008).
- A. D. Webb, R. N. Dixon and M. N. R. Ashfold, *J. Chem. Phys.* **127**, 224307 (2007).

A. D. Webb, N. H. Nahler and M. N. R. Ashfold, *J. Phys. Chem. A* **113**, 3773-3778 (2009).

H. J. Werner, P. J. Knowles, G. Knizia, F. R. Manby and M. Schutz, *WIREs Comput. Mol. Sci* **2**, 242-253 (2012).

*MOLPRO, version 2015.1, a package of ab initio programs*, H. J. Werner, P. J. Knowles, G. Knizia, F. R. Manby, M. Schutz and others.

C. M. Western, *J. Quant. Spec. Radiat. Transfer* **186**, 221-242 (2016).

*pGopher, A Program for Simulating Rotational, Vibrational and Electronic Spectra*, C. M. Western, (University of Bristol, 2015).

H. Xu, Y. Guo, Q. Li, Y. Shi, S. Liu and X. Ma, *J. Chem. Phys.* **121**, 3069-3073 (2004).

H. Xu, Y. Guo, S. Liu, X. Ma, J. Liang and H. Li, *J. Chem. Phys.* **119**, 11609-11614 (2003).

K. Yoshizawa, Y. Shiota and T. Yamabe, *J. Am. Chem. Soc.* **120**, 564-572 (1998).

K. A. Zemski, D. R. Justes and A. W. Castleman, *J. Phys. Chem. B* **106**, 6136-6148 (2002).